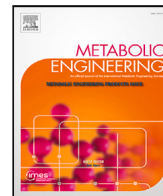




Contents lists available at ScienceDirect

## Metabolic Engineering

journal homepage: [www.elsevier.com/locate/meteng](http://www.elsevier.com/locate/meteng)

Original Research Article



## Multi-omics driven genome-scale metabolic modeling improves viral vector yield in HEK293

L. Zehetner<sup>a,b</sup>, D. Széliová<sup>a</sup>, B. Kraus<sup>d</sup>, J.A. Hernandez Bort<sup>c</sup>, J. Zanghellini<sup>a</sup><sup>a</sup> Department for Analytical Chemistry, University of Vienna, Vienna, 1090, Austria<sup>b</sup> Doctoral School of Chemistry, University of Vienna, Vienna, 1090, Austria<sup>c</sup> Department of Applied Life Sciences, Bioengineering, University of Applied Sciences Campus Vienna, Vienna, 1100, Austria<sup>d</sup> Institute of Molecular Biotechnology, Institut für Molekulare Biotechnologie GmbH, Vienna, 1030, Austria

## ARTICLE INFO

Dataset link: [Improving HEK293-based AAV-production using GSMMs, and a multi-omics approach \(Original data\)](#)

## Keywords:

GSMM  
HEK293  
AAV  
Bioprocess  
HIF-1 $\alpha$ 

## ABSTRACT

HEK293 cells are a versatile cell line extensively used in the production of recombinant proteins and viral vectors, notably Adeno-associated virus (AAV) (Bulcha et al., 2021). Despite their high transfection efficiency and adaptability to various culture conditions, challenges remain in achieving sufficient yields of active viral particles. This study presents a comprehensive multi-omics analysis of two HEK293 strains under good manufacturing practice conditions, focusing on the metabolic and cellular responses during AAV production. The investigation included lipidomic, exometabolomic, and transcriptomic profiling across different conditions and time points. Genome-scale metabolic models (GSMMs) were reconstructed for these strains to elucidate metabolic shifts and identify potential bottlenecks in AAV production. Notably, the study revealed significant differences between a High-producing (HP) and a Low-producing (LP) HEK293 strains, highlighting pseudohypoxia in the LP strain. Key findings include the identification of hypoxia-inducible factor 1-alpha (HIF-1 $\alpha$ ) as a critical regulator in the LP strain, linking pseudohypoxia to poor AAV productivity. Inhibition of HIF-1 $\alpha$  resulted in immediate cessation of cell growth and a 2.5-fold increase in viral capsid production, albeit with a decreased number of viral genomes, impacting the full-to-empty particle ratio. This trade-off is significant because it highlights a key challenge in AAV production: achieving a balance between capsid assembly and genome packaging to optimize the yield of functional viral vectors. Overall this suggests that while HIF-1 $\alpha$  inhibition enhances capsid assembly, it simultaneously hampers nucleotide synthesis via the pentose phosphate pathway (PPP), necessary for nucleotide synthesis, and therefore for AAV genome replication.

## 1. Introduction

Human embryonic kidney 293 (HEK293) is a highly adaptable cell line originating from human embryonic kidney cells cultivated in tissue culture. Developed in 1977 (Graham et al., 1977), HEK293 cells have become pivotal in the generation of recombinant proteins (Thomas and Smart, 2005; Dietmair et al., 2012; Malm et al., 2020; Abaandou et al., 2021) and viral vectors (Bulcha et al., 2021; Strasser et al., 2021; Catalan-Tatjer et al., 2024; Zehetner et al., 2023), owing to their high transfection efficiency and robust proliferation. At least 564 distinct HEK293 strains are documented (Bairoch, 2018), each optimized for specific applications. These cells are widely used in the biopharmaceutical sector to produce recombinant proteins not effectively expressed in Chinese Hamster Ovary (CHO) cells (Malm et al., 2022). A significant advantage of HEK293 cells is their adaptability to diverse culture conditions; they are capable of growing in both

suspension and adherent cultures (Malm et al., 2020; Lin et al., 2014) and are suitable for serum-free media, which facilitates scalable and reproducible production processes.

HEK293 cells are widely used for producing viral vectors essential for cell and gene therapy (Blessing et al., 2019; Pistek et al., 2023; Kahlig et al., 2024), and vaccine development (Joe et al., 2022; Chen et al., 2018b). These vectors include lentiviruses, adenoviruses, and AAV (Bulcha et al., 2021), with AAV especially prominence in *in vivo* gene therapy, leading to six approved drugs in recent years (Catalan-Tatjer et al., 2024). Despite their therapeutic potential, producing sufficient active viral particles remains challenging due to high associated costs, and the fact that only 10% of the AAV contain the gene of interest in full length (Moço et al., 2023; Mendes et al., 2022). Thus, many studies have aimed at enhancing AAV titers in

\* Corresponding authors.

E-mail addresses: [Leopold.Zehetner@univie.ac.at](mailto:Leopold.Zehetner@univie.ac.at) (L. Zehetner), [diana.szeliova@univie.ac.at](mailto:diana.szeliova@univie.ac.at) (D. Széliová), [juan\\_antonio.hernandez\\_bort@fh-campuswien.ac.at](mailto:juan_antonio.hernandez_bort@fh-campuswien.ac.at) (J.A. Hernandez Bort), [juergen.zanghellini@univie.ac.at](mailto:juergen.zanghellini@univie.ac.at) (J. Zanghellini).<https://doi.org/10.1016/j.ymben.2025.03.011>

Received 10 October 2024; Received in revised form 6 February 2025; Accepted 19 March 2025

Available online 11 April 2025

1096-7176/© 2025 The Authors. Published by Elsevier Inc. on behalf of International Metabolic Engineering Society. This is an open access article under the CC BY license (<http://creativecommons.org/licenses/by/4.0/>).

**Table 1**  
Overview of recently performed -omics based studies of HEK293 strains during AAV production.

HEK293 strain	Medium	Set up	Data	Reference
ATCC: CRL-1573	AMBIC	shake flask	Transcriptome	Wang et al. (2023)
Mass Biologics, Inc.	BalanCD	shake flask	Transcriptome	Wang et al. (2023)
unknown origin	FreeStyle F17	50L bioreactors	Transcriptome	Chung et al. (2023)
FreeStyle 293F	BalanCD	shake flask	Proteome	Strasser et al. (2021)
Cell Biolabs, Inc.	DMEM (+10% FBS)	T-flask	Transcriptome, Proteome	Lu et al. (2024)
Expi293	HE400AZ	Erlenmeyer flask	Transcriptome	Shiina et al. (2022)
ATCC: CRL-1573 (LP)	FreeStyle F17	250mL bioreactors	Transcriptome	Pistek et al. (2023)
HP	FreeStyle F17	250mL bioreactors	Transcriptome	Pistek et al. (2023)

HEK293 cells (Blessing et al., 2019; Clement and Grieger, 2016). Beyond optimizing process parameters, several studies have examined the cellular behavior of HEK293 cells using single-omics datasets during growth (Malm et al., 2020; Dietmair et al., 2012; Martinez-Monge et al., 2019) or production (Malm et al., 2022; Strasser et al., 2021; Dietmair et al., 2012; Quek et al., 2014; Shiina et al., 2022; Wang et al., 2023; Pistek et al., 2023), as summarized in Abaandou et al. (2021).

The behavior of host cells during AAV production has been extensively studied using transcriptomes (Wang et al., 2023; Pistek et al., 2023; Kahlig et al., 2024), proteomes (Strasser et al., 2021; Shiina et al., 2022), or both (Lu et al., 2024) (Table 1), as recently summarized (Gurazada et al., 2024). Despite variations in fermentation conditions, strains, and AAV serotypes, two pathways were consistently enriched during production: (i) endoplasmic reticulum (ER) stress and the unfolded protein response (UPR) (Kahlig et al., 2024; Pistek et al., 2023; Wang et al., 2023; Lu et al., 2024; Strasser et al., 2021), and (ii) immune response (Shiina et al., 2022; Kahlig et al., 2024; Wang et al., 2023; Lu et al., 2024). ER stress occurs when unfolded or misfolded proteins accumulate in the ER, triggering the UPR to restore ER homeostasis. Key proteins involved in UPR activation include GRP78, ATF6, PERK, and IRE1. PERK phosphorylates *eIF2 $\alpha$* , thereby inhibiting CAP-dependent protein translation (Madden et al., 2019). ER stress and UPR are common challenges in recombinant protein production (Castellano et al., 2023; Prashad and Mehra, 2015), so their upregulation in HEK293 during AAV production is expected. Additionally, transcriptomic analyses identified the JAK-STAT signaling pathway as central during AAV production in HEK293 strains (Wang et al., 2023; Kahlig et al., 2024). This pathway mediates the innate immune response to viral infections and regulates genes involved in antiviral defense, inflammation, cell growth, and differentiation (Hu et al., 2021; O'Shea et al., 2015; Ezeonwumelu et al., 2021). Inhibiting *STAT1* with Ruxolitinib led to a two-fold titer increase in shake flasks and a 50% improvement in a 3L bioreactor (Kahlig et al., 2024). However, in certain HEK293 strains (Kahlig et al., 2024), the JAK-STAT pathway was upregulated even before transfection, indicating a pre-existing stressed state, while in others, it was either triggered by AAV production (Wang et al., 2023) or downregulated by ethanol addition (Shiina et al., 2022). The cause of this immune response, whether due to HEK293 strain adaptation or AAV particle production, remains unclear.

Differences in immune responses prior to transfection could arise from variations between suspension and adherent culturing of HEK293 strains. Jang et al. (2022) recently highlighted metabolic differences after adapting an adherent HEK293 strain to suspension culture. The study found increased glucose uptake, lactate secretion, and succinate production in HEK293 cells adapted to suspension culture, suggesting that these cells experience pseudohypoxia (Hayashi et al., 2019). In CHO cells, reducing pseudohypoxia by inhibiting pyruvate dehydrogenase kinase with dichloroacetate has been shown to improve culture performance, and antibody production (Buchsteiner et al., 2018).

Viral vectors may influence host cell metabolism more directly, similar to how viruses reprogram host metabolism to support their replication (Thaker et al., 2019). This is especially relevant for AAV production, which relies on helper functions from other viruses, like

Adenovirus (Meier et al., 2020; Nie et al., 2024), or Herpesvirus (Feudner et al., 2001; Alazard-Dany et al., 2009). While the impact of viral genes, such as *E4ORF1* from Human adenovirus (Thai et al., 2014), on host metabolism has been studied, the metabolic effects during AAV replication remain largely unexplored and could be investigated using genome-scale metabolic modeling (Zehetner et al., 2023).

GSMMs are mathematical representations of cellular metabolism, first developed over two decades ago (Edwards and Palsson, 1999). Since then, more than 1000 GSMMs have been reconstructed across all domains of life (Gu et al., 2019). In bioprocess engineering, GSMMs have provided deep insight at a cellular level leading to improved growth and production behavior in microbes (Schlögel et al., 2024; Gotsmy et al., 2024, 2023; Cotner et al., 2021; Vailionis et al., 2023; Xu et al., 2009; Aminian-Dehkordi et al., 2019) and mammalian cells (Huang et al., 2020; Chen et al., 2019; Pérez-Fernández et al., 2021). However, currently, there are no GSMM for HEK293 cells during Recombinant protein (RP) or viral particle production. Existing HEK293 models are small-scale, focusing on selected pathways or AAV production via triple transfection (Zehetner et al., 2023). The most detailed HEK293 GSMM includes 357 reactions and was manually curated for RP production (Quek et al., 2014) using transcriptomic and exometabolomic data (Dietmair et al., 2012) based on the Recon2 model (Swainston et al., 2016).

Meanwhile, reconstructions of human metabolism have been continuously refined and updated (Robinson et al., 2020; Brunk et al., 2018), allowing the use of computational tools to automatically generate cell-specific GSMMs (Jerby et al., 2010; Becker and Palsson, 2008; Agren et al., 2012; Vlassis et al., 2014; Schultz and Qutub, 2016). However, obtaining accurate condition-specific GSMMs, requires integrating additional constraints, such as enzyme limitations (Chen et al., 2024), thermodynamic constraints (Salvy et al., 2019), and constraints on exchange reactions (Széliová et al., 2020, 2021) or biomass composition (Széliová et al., 2020; Choi et al., 2023; Bernstein et al., 2021). Experimental data on exchange rates and biomass' dry weight, are pivotal but can disrupt simulations (Széliová et al., 2020) if not precisely measured (Széliová et al., 2021). Similarly, macromolecular biomass composition, particularly the lipidome, varies under different environmental conditions and strongly influences predicted flux distributions (Choi et al., 2023; Bernstein et al., 2021). Thus, understanding exometabolites and biomass composition – especially the lipidome – is essential for modeling viral vector production. Unfortunately, such data are currently unavailable for AAV producing HEK293 cells.

In this study, we conducted a multi-omics analysis of two HEK293 strains, which were partially examined in previous research for AAV production (Pistek et al., 2023; Kahlig et al., 2024). Using the latest reconstruction of human metabolism (Robinson et al., 2020), we developed 20 condition-specific GSMMs from the two strains, analyzing mock and transfected conditions across five time points with four biological replicates each. We find that over 99.8% of cellular resources in both strains are used for growth rather than AAV production. To reallocate the resources, we aimed to inhibit growth and therefore increase AAV production in the LP strain. With the multi-omics analysis – encompassing lipidomes, transcriptomes, and fluxomes – we identified HIF-1 $\alpha$  as a potential target in the LP strain, suggesting that the LP

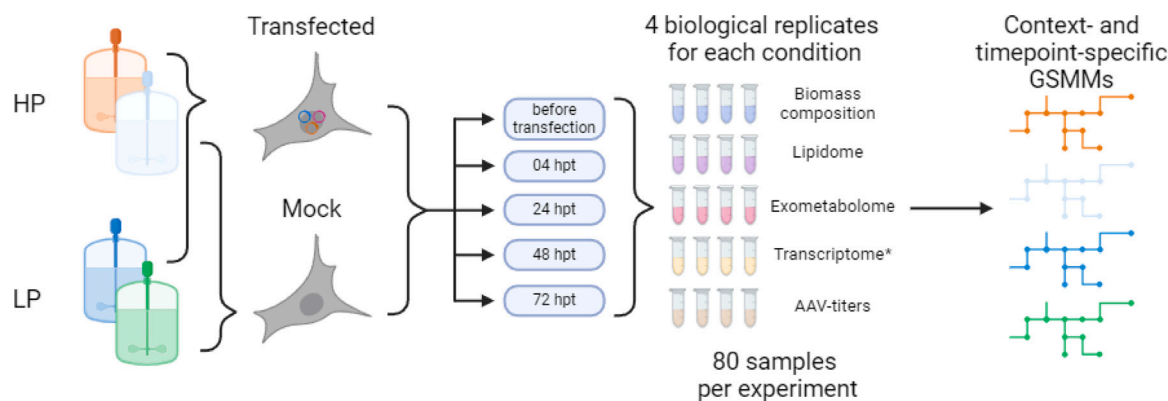


Fig. 1. Graphical overview of the methods section. All samples were measured as described in the methods. Transcriptomic data were obtained from (Pistek et al., 2023).

strain is affected by pseudohypoxia due to recent adaption from adherent to suspension culturing. Inhibiting HIF-1 $\alpha$  halted cellular growth and improved the specific productivity of viral capsids by over two-fold. However, the number of viral genomes decreased following HIF-1 $\alpha$  inhibition, leading to a less favorable full-empty ratio. Despite this, our study provides a comprehensive multi-omics analysis and represents a significant advancement in data-driven process design. Overall, our study provides valuable insights into the metabolic behavior of different HEK293 strains during AAV production. Rather than employing GSMs as predictive tools, we utilized them as platforms for data integration and analysis. Despite certain limitations, this work offers a comprehensive multi-omics analysis and constitutes an important advancement toward data-driven process design.

## 2. Materials and methods

### 2.1. Bioprocess and sampling

The bioprocess from cell culture to fermentation was performed as described recently by Pistek et al. (2023). Briefly, two distinct HEK293 suspension cell line strain stocks, stored at  $-130\text{ }^{\circ}\text{C}$ , were cultured at  $37\text{ }^{\circ}\text{C}$  in chemically defined, serum-free medium (FreeStyle F17, ThermoFisher, NY, USA) supplemented with  $8\text{ mM}$  L-Glutamine and  $1.0\text{ gL}^{-1}$  Lutrol. The cultivation was carried out in a HERA Cell 150 (Thermo Fisher Scientific) incubator with  $5\%$   $\text{CO}_2$ . To enhance statistical analysis, each cell line was cultivated in four biological replicates using Single Use Spinner flasks (Corning, Germany), with volumes ranging from  $61\text{ mL}$  to  $1600\text{ mL}$  during the cell expansion phase. After 12 days, the cells were transferred to an ambr250 Modular fermentation system (Sartorius, Germany) under controlled conditions ( $\text{pH}$ ,  $\text{CO}_2$ ,  $\text{O}_2$ ) for transient AAV 8 particle production. Prior to transfection, cells were diluted to a uniform density of  $4.0 \cdot 10^6$  cells per mL to facilitate comparison. Each biological replicate was divided into two fermentation vessels: one for plasmid transfection and the other for mock transfection (without plasmids). A triple-plasmid transfection was performed using Polyethylenimine (Merck KGaA, Darmstadt, Germany), containing Adenovirus 5 Helper genes, Rep2Cap8, and a transgene sequence, in accordance with the supplier's instructions. Post-transfection, cells were cultured for  $72\text{ h}$  at  $37\text{ }^{\circ}\text{C}$  and sampled for analysis at five different time points: before (0 HPT) and after transfection (4, 24, 48, and 72 HPT), resulting in a total of 80 samples (see Fig. 1). Additional samples were taken at 21, 27, 45, and 51 HPT for quantification of lactate, ammonia (BioHT), proline, and glycine.

### 2.2. Experimental analyses

#### 2.2.1. Biomass and cell count

As described in Széliová et al. (2020),  $1\text{ mL}$  of cell suspension was centrifuged at  $200\text{ g}$  for  $10\text{ min}$  at  $4\text{ }^{\circ}\text{C}$ . The pellet was then washed with  $1\text{ mL}$  of pre-cooled phosphate-buffered saline (PBS,  $1\text{ M}$ ,  $4\text{ }^{\circ}\text{C}$ ). To protect the cells during subsequent steps, Pluronic™ F-68 Non-ionic Surfactant (Gibco™, MA, USA) was added to the suspension at a final concentration of  $2\%$  (v/v). Glass beakers and silica beads were prepared by drying them overnight at  $90\text{ }^{\circ}\text{C}$ . They were subsequently cooled in a vacuum desiccator for  $20\text{ min}$  before being weighed to ensure accuracy. Each sample, resuspended in a  $1\text{ M}$  PBS solution, was transferred to the pre-weighed beakers. The samples were then dried at  $90\text{ }^{\circ}\text{C}$  until the biomass remained constant, ensuring complete removal of moisture. Before each weighing, the beakers were cooled for  $20\text{ min}$  in the vacuum desiccator to prevent heat-related measurement inaccuracies. Cell counts were performed using a NucleoCounter202 (Allerod, Denmark), adhering strictly to the manufacturer's protocol.

#### 2.2.2. Cellular glucose content

In alignment with the methodology described by Széliová et al. (2020), we posited glucose as the predominant carbohydrate component within the cells and thus limited our carbohydrate quantification to glucose. For this purpose, we employed the Total Carbohydrate Quantification Assay Kit (ab155891, Abcam, Cambridge, UK). Beginning with cell pellets containing  $3\text{--}10 \cdot 10^6$  cells, we adjusted the volume of lysis buffer proportionately. Sample preparation was carried out following the manufacturer's instructions. Each sample was analyzed in technical triplicates to enhance the reliability of our measurements.

#### 2.2.3. Cellular DNA and RNA content

DNA and RNA content was extracted from the same sample using the AllPrep DNA/RNA Mini Kit (Qiagen, Venlo, NE). As suggested by the manufacturer,  $\beta$ -mercaptoethanol (Thermo Fisher Scientific Inc., Waltham, MA, US) was added to inhibit RNases. Samples were quantified on a Nanodrop 2000 (Thermo Fisher Scientific Inc., Waltham, MA, US) in technical triplicates.

#### 2.2.4. Cellular protein content

Cell pellets were lysed by adding lysis buffer (PreOmics, Martinsried, GER), followed by incubation on a preheated thermocycler ( $95\text{ }^{\circ}\text{C}$ ,  $10\text{ min}$ ,  $1000\text{ rpm}$ ). Protein content was then quantified using the Qubit protein broad range assay kit (Thermo Fisher Scientific Inc., Waltham, MA, US) following the manufacturer's instructions.

### 2.2.5. Cellular lipidome

For extraction, one aliquote in 2 mL Eppendorf vessel, each containing  $3 - 10 \cdot 10^6$  cells were used. 205  $\mu\text{L}$  of cold Methanol (Thermo Fisher Scientific Inc., Waltham, MA, US) were added to the cells, and they were vortexed for 20 s. As labeled internal lipid standards, 10  $\mu\text{L}$  Splash Mix undiluted, 10  $\mu\text{L}$  Ceramide Mix undiluted, and 10  $\mu\text{L}$  Cardiolipin Mix undiluted were added (Avanti Polar Lipids, Alabaster, AL, US) to each sample. Further, the samples were allowed to thaw at room temperature and were sonicated for 10 min at 4 °C. Then, 750  $\mu\text{L}$  of Methyl-tert-butyl-ether (Thermo Fisher Scientific Inc., Waltham, MA, US) were added, and the mixture was incubated for 1 h at room temperature under agitation. Phase separation was induced by adding 188  $\mu\text{L}$  water with 0.1% ammonium formate (Thermo Fisher Scientific Inc., Waltham, MA, US). The extract was centrifuged at 10,000 g for 5 min, and two 200  $\mu\text{L}$  aliquots of the upper phase were collected in another 2 mL Eppendorf vessel, dried in a vacuum centrifuge, and stored if necessary at  $-20$  °C. For further analyses, samples were dissolved in 200  $\mu\text{L}$  2-Propanole/Methanole/Chloroform (4:2:1, v/v/v) containing 7.5 mM ammonium formate. LC-MS measurements were performed as described by Schoeny et al. (2020). A high field Q Exactive HF™ quadrupole-Orbitrap mass spectrometer (Thermo Fisher Scientific) was connected with a robotic nanoflow ion source TriVersa NanoMate® (Advion BioSciences, Ithaca NY, USA) and a nanoelectrospray ionization (nanoESI) chip with spraying nozzles of 5  $\mu\text{m}$  nominal internal diameter. Samples were placed in a 96 twin.tec® well plate (Eppendorf, Hamburg, Germany). Following settings were applied in the Chipsoft 8.3.1 software (Advion BioSciences): ionization voltage 1.25 kV (pos)/ $-1.25$  kV (neg); backpressure 0.9 psi and in the MS source parameters: capillary temperature 250 °C, S-Lens radio frequency level 50. A 9 min polarity switching method with data independent acquisition (DIA) and MS1 scans was used with the following settings: resolution 240,000 (MS1), 60,000 (MS2), AGC target 1e6 (MS1), 2e5 (MS2), maximum IT 150 ms (MS1), 130 (MS2), scan range in MS1 m/z 350-1,050 (pos)/m/z 200-1,200 (neg), NCE for MS2 of 21 (pos)/ 26 (neg) and a fixed first mass of m/z 80 (pos)/ m/z 150 (neg). LipidXplorer 1.2.8 settings were the following: mass tolerance 5 ppm, min. occupation of 0. In positive mode: intensity threshold 70,000 (MS1)/ 1,000 (MS2), resolution 230,000 (MS1)/ 60,000 (MS2), resolution gradient  $-180$  (MS1)/ $-40$  (MS2). In Negative mode: intensity threshold 60,000 (MS1)/ 1,000 (MS2), resolution 260,000 (MS1)/ 80,000 (MS2), resolution gradient  $-170$  (MS1)/  $-100$  (MS2). Identified lipids were removed if the absolute mass error was above 3, if isobaric compounds were present and if the concentration was below LOQ (limit of quantification). LOQ values were calculated by multiplying the standard deviation of 5 repetitive injections of a low concentrated Splash ISTD with 10. For quality control, a 10  $\mu\text{L}$  plasma sample aliquot, which was placed at RT in a 2 mL Eppi, 290  $\mu\text{L}$  Methanol, 10  $\mu\text{L}$  Splash Mix I (undiluted), 1.000  $\mu\text{L}$  methyl-tert-butyl-ether were added. The mixture was shaken for 1 h at RT. Phase separation was induced by adding 250  $\mu\text{L}$  of MS-grade water. Upon 10 min of incubation at room temperature, the sample was centrifuged at 1,000 g for 10 min. The upper (organic) phase was collected in another 2 mL Eppi and dried in the SpeedVac. The dried lipids were dissolved in 200  $\mu\text{L}$  isopropyl alcohol for LC-MS injection.

### 2.2.6. Estimated metabolite pool from human1 biomass reaction

To partially account for the undefined part of the biomass composition, we obtained the metabolites of the metabolites pool from human1 (Robinson et al., 2020), and calculated the amount estimated amount of metabolites of the measured dry weight, as described in Széliová et al. (2020).

### 2.2.7. Spent media analysis

**LC-MS based metabolomics** 1 mL suspension was centrifuged (200 g, 8 min, 4 °C), from which 100  $\mu\text{L}$  liquid media was placed into a 2 mL Eppendorf vessel, and kept on ice. 50  $\mu\text{L}$  of yeast internal standard (ISTD) (extract out of 2 billion cells reconstituted in 2 mL water), and

600  $\mu\text{L}$  methanol were added to reach a final volume of 750  $\mu\text{L}$  (80% methanol, v/v), which resulted in a 1:7.5 dilution of the sample and a 1:15 dilution of the ISTD. After thorough vortexing, it was kept on ice for 30 min. Then it was vortexed again and kept at  $-20$  °C overnight. The samples were centrifuged (14,000 g, 4 °C, 15 min) and two 200  $\mu\text{L}$  aliquots were dried in a vacuum centrifuge. They were stored if necessary at  $-20$  °C. Shipping should be done on dry ice. At least 20-50  $\mu\text{L}$  aliquots of the yeast ISTD (extract out of 2 billion cells reconstituted in 2 mL water) should be placed into 2 mL Eppendorf vessels for internal standardization of the calibrators and QC samples. These samples were also dried in a vacuum centrifuge. All samples were dissolved in 200  $\mu\text{L}$  20% water/80% acetonitrile (v/v). Vigorously vortexed for 3 min to ensure complete dissolving of the sample and centrifuged (14,000 g, 4 °C, 10 min) prior to being transferred to an HPLC vial. LC-MS measurements were performed as described in Schoeny et al. (2020). A Vanquish™ Horizon HPLC (Thermo Fisher Scientific) with an iHILIC®-(P) Classic (2.1 mm  $\times$  100mm, 5  $\mu\text{m}$ , HILICON, Umea, Sweden) was used for hydrophilic interaction liquid chromatography-high resolution mass spectrometry (HILIC-HRMS). The flow rate was set to 200  $\mu\text{L}$  min $^{-1}$  and the column temperature to 40 °C. Solvent A was 90% 15 mM ammonium acetate (pH 9.4), 10% acetonitrile, and solvent B was 90% acetonitrile, 10% 15 mM ammonium acetate (pH 9.4). The following gradient was used: 0–12 min ramp from 100% B to 20% B, 12–14 min 20%, 14–17 min ramp to 0% B, 17–19 min 0% B and 20–27 min 100% B as equilibration step. The injection volume was 5  $\mu\text{L}$  and the injector needle was washed with acetonitrile: methanol: water 1:1:1 (v/v/v) for 5 s after each injection. A high field Q Exactive HF™ quadrupole-Orbitrap mass spectrometer (Thermo Fisher Scientific) was used as MS. The following source parameters were applied in both polarities in polarity switching mode: capillary temperature of 280 °C, sheath gas flow rate of 40, an auxiliary flow rate of 3, sweep gas of 0, S-lens RF level of 30 and auxiliary gas heater temperature of 320 °C applying a spray voltage of 3.5 kV in positive mode and 2.8 kV in negative mode. In MS1 mode the mass range in both polarities was set to m/z 60–900 A maximum IT of 100 ms, a resolution of 120,000, and an AGC target of  $3 \cdot 10^6$  was applied. Skyline (version 22.2.0.312) was used for peak integration and R/ R studio for final data processing. Identified lipids were removed if the absolute mass error was above 3 and if the concentration was below LOQ. LOQ was defined as the lowest standard concentration in the linear range. For calibration one dried ESTD stock solution is dissolved in 200  $\mu\text{L}$  water for a final conc. of 50  $\mu\text{M}$ . 14 calibrants with concentrations from 25  $\mu\text{M}$  to 0.001  $\mu\text{M}$  were prepared. The internal standard is already dried in the Eppi, therefore the standards are vortexed, centrifuged, and transferred to the well plate.

**Proline and Glycine** Results for proline and glycine showed inconsistent results. Therefore, these amino acids were quantified using Waters AccQ tagging (Milford, MA, USA) at nine different time points. Briefly, spent media samples were filtered by centrifugation (10 min, RT, 12,000 g) using 3 K Amicon (Merck KGaA, Darmstadt, GER) filters to remove proteins. The flowthrough was diluted 1:10 (MilliQ Water) and labeled together with calibration standards according to the manufacturer's instructions. Norvaline was used as internal standard for normalization. Waters Acquity (UPLC03, Milford, MA, USA) was used as HPLC system. The mobile phase consisted of Eluent A (1:10 diluted in MilliQ Water) and Eluent B (undiluted). For every sample the runtime was set to 11 min with a flowrate of 0.7 mL/min. The gradient of Eluent B was increased from 0.1% at the beginning to 90%.

**Lactate and Ammonia** Lactate and Ammonia were quantified from supernatant for 9 time points. Samples were centrifuged (10 min, 200 g, 4 °C) and measured on a BioHT (Roche, Switzerland), following the manufacturer's instructions. From spent media analyses, limiting compounds were determined, that were fully consumed first. These limiting compounds were then added as supplements to improve the bioprocess.

### 2.2.8. Quantification of AAV

**Droplet digital PCR** As described by Pistek et al. (2023), for quantifying vector genomes, a droplet digital PCR method from Bio-Rad was employed using the fully automated QX One System (Hercules, CA, USA), which allows for absolute quantification of vector genomes without the need for standard curves. The sample is partitioned into oil droplets, with each droplet serving as an independent PCR reaction compartment. During the initial phase of PCR in the thermal cycler, capsids are degraded, making the DNA accessible for amplification. The vector genome titer is then determined using a droplet reader. To remove extraneous DNA sequences, samples were treated with DNase I (NEB, Ipswich, MA, USA). Prior to this treatment, samples were pre-diluted to enhance the efficiency of DNase I activity. Following droplet generation, PCR was conducted with Bio-Rad ddPCR Supermix (no dUTP) and transgene-specific primers and probe.

**ELISA** As described by Pistek et al. (2023), an AAV8 titration ELISA kit (Progen, Heidelberg, GER) was used for quantifying AAV8 capsids, utilizing a monoclonal antibody (ADK8) that recognizes a specific conformational epitope on the assembled AAV8 capsids. The captured AAV 8 particles were identified by the binding of biotinylated anti-AAV 8 ADK8, as this epitope is consistently presented on the AAV 8 capsid structure. Streptavidin peroxidase and a peroxidase substrate were subsequently applied to measure the amount of bound anti-AAV 8, thus indicating the concentration of AAV 8 capsids. The resulting color change was measured at 450 nm using a photometer. The kit also includes an AAV 2/8 particle preparation with a known concentration of labeled AAV 8 particles for calibration purposes.

## 2.3. Computational analyses

### 2.3.1. Lipidome analysis

PCA was performed on the lipidomic dataset was performed using the prcomp function in RStudio with the parameters center, and scale set to TRUE. Prior to that, every sample was normalized by dividing each lipid by the total amount of lipid in this sample. Loadings, obtained from PCA, were grouped by lipid class. The five longest loading vectors (lipid classes) were displayed in the PCA plot as well to identify the drivers behind the separation of the samples.

### 2.3.2. Calculation of experimental growth rates during non-exponential growth and production phase

The (specific) growth rate was calculated by:

$$\mu_t = \frac{1}{x_t} \frac{dx_t}{dt} \quad (1)$$

where  $\mu_t$  is the growth rate at time point  $t$ ,  $x_t$  is the biomass value derived from the fitted function  $x$ , and  $\dot{x}_t$  is the derivative of  $x_t$ . A logistic function

$$x = \frac{a}{1 + \exp[-b(t - c)]} \quad (2)$$

was used for fitting the biomass.

The error of the growth rate was calculated by:

$$\mu_t^{err} = \sqrt{\left(\frac{\dot{x}_t^{err}}{x_t}\right)^2 + \left(-\mu_t \frac{x_t^{err}}{x_t}\right)^2} \quad (3)$$

where  $\mu_t^{err}$  is the error of the growth rate at time point  $t$ ,  $\dot{x}_t^{err}$  is the error of the derivative value, and  $x_t^{err}$  is the error of the fitted biomass value.  $x_t^{err}$  and  $\dot{x}_t^{err}$  were obtained by:

$$x_t^{err} = \sqrt{\left(\sum_{j=1}^3 \frac{\partial x_t}{\partial \theta_j} \cdot \theta_j^{err}\right)^2} \quad (4)$$

and

$$\dot{x}_t^{err} = \sqrt{\left(\sum_{j=1}^n \frac{\partial \dot{x}_t}{\partial \theta_j} \cdot \theta_j^{err}\right)^2} \quad (5)$$

where  $\theta_j$  is a parameter in the logistic fitting function  $x$ , and  $\theta_j^{err}$  is its corresponding error value from the fitting function  $h$ .

Derivatives were calculated in R, using the package Deriv (v4.1) (Clausen and Sokol, 2020)

### 2.3.3. Calculation of exchange rates

From the analysis of spent media, we identified 32 metabolites based on their concentration profiles, from which exchange rates could be calculated. These metabolites were categorized into three groups according to the fitting function applied. Specifically, 27 metabolites were fitted using an exponential function, 4 were fitted using a quadratic function, and 1 metabolite was fitted using a cubic function, employing robust fitting techniques (R function nlrob). To determine the exchange rates at each timepoint post-transfection, the derivative of the fitted function was calculated. Error propagation was then performed following the appropriate equation to ensure accurate quantification of exchange rates.

The exchange rate  $q_{i,t}$  of metabolite  $i$  was calculated as

$$q_{i,t} = \frac{\dot{f}_{i,t}}{x_t} \quad (6)$$

where  $\dot{f}_{i,t}$  is the derivative value of the fitted function  $f_i$  for metabolite  $i$  at timepoint  $t$ . The error of  $q_{i,t}$  is calculated by error propagation following:

$$q_{i,t}^{err} = \sqrt{\left(\frac{1}{x_t} \cdot \dot{f}_{i,t}^{err}\right)^2 + \left(-\frac{\dot{f}_{i,t}}{x_t^2} \cdot x_t^{err}\right)^2} \quad (7)$$

where  $q_{i,t}^{err}$  is the error of  $q_{i,t}$  for metabolite  $i$  at timepoint  $t$ ,  $\dot{f}_{i,t}^{err}$  is the error obtained from the derivative  $\dot{f}_i$  of the fitted function  $f_i$ . The derivative  $\dot{f}_i$  of the fitted function  $f_i$  was obtained by

$$\dot{f}_i = \frac{df_i}{dt} \quad (8)$$

The corresponding error  $\dot{f}_{i,t}^{err}$  was calculated by:

$$\dot{f}_{i,t}^{err} = \sqrt{\left(\sum_{j=1}^n \frac{\partial \dot{f}_{i,t}}{\partial \theta_j} \cdot \theta_j^{err}\right)^2} \quad (9)$$

where  $\partial \dot{f}_{i,t}$  is the partial derivative of the derivative  $\dot{f}_{i,t}$  for metabolite  $i$  at timepoint  $t$  with respect to the parameter  $\theta_j$ .  $\theta_j^{err}$  is the obtained error of every parameter  $\theta_j$  in the fitted function  $f_i$  with  $n$  parameters. To obtain fitted functions  $f_i$ , the nlrob function in R was used to fit one of the three different functions:

$$f_{1,i} = a \cdot b^t \quad (10)$$

for metabolites, showing an exponential concentration profile,

$$f_{2,i} = a \cdot t^2 + b \cdot t + c \quad (11)$$

for metabolites, showing a quadratic concentration profile (lactate, proline, and glycine), or,

$$f_{3,i} = a \cdot t^3 + b \cdot t^2 + c \cdot t + d \quad (12)$$

for ammonium, showing a cubic concentration profile.

To consider natural degradation rate of glutamine, media was sampled daily. Glutamine and ammonia were quantified on the BioHT (Roche, Switzerland). The natural degradation rate was calculated using an exponential fit  $f_{1,i}$ . The obtained depletion rate was subtracted from the derivative value  $\dot{f}_{i,t}$  for glutamine or added to the derivative value  $\dot{f}_{i,t}$  for ammonia.

### 2.3.4. Reconstruction of context-specific models

To reconstruct context-specific GSMs, the most recent GSMM of the human metabolism, human1 (Robinson et al., 2020), was used. Initially, the uptakes of 42 compounds were identified to enable feasible solutions of the GSMM. These compounds were selected based on

a chemically defined medium (22400 - RPMI 1640, HEPES, Thermo Fisher Scientific Inc., Waltham, MA, USA), since the exact composition of the used F17 expression media is currently not available. Additionally, all compounds identified by Daskalaki et al. (2018) that are not essential for growth were included as potential secretion reactions, totaling 23 compounds. Moreover, metabolites for which exchange rates could be calculated (as detailed in the subsequent section) were incorporated into the model as constraints. The compounds in the growth medium were assigned exchange reaction boundaries of  $[-1,000, 0]$ , while the boundaries for all other exchange reactions were set to  $[0, 1,000]$ .

To obtain context-specific GSMMs, transcriptomic data from the exponential growth phase were utilized as reported in Dietmair et al. (2012). This transcriptomic dataset, derived from a non-producing strain, encompasses four time points during exponential growth, with transcriptomes sequenced in triplicates. For each sample, GSMMs were reconstructed using the CORDA algorithm (v 0.4.2) (Schultz and Qutub, 2016). We generated five subsets of expressed genes for each sample, corresponding to the top 10%, 25%, 50%, 75%, and 90% of the highest expressed genes. Using these subsets, reactions were identified based on gene-reaction rules. A reaction with assigned isoenzymes (“OR” in the gene-reaction rule) was identified to be active, if one of the associated genes were in the selected list of genes. A reaction with assigned enzyme complexes (“AND” in the gene-reaction rule) was included, if all of the associated genes were in the selected list of genes. Reactions associated with genes in each subset were assigned a confidence score of 3, indicating the highest certainty in the CORDA framework. Additionally, reactions essential for biomass production, and exchange reactions of medium compounds and potential secretory metabolites (Daskalaki et al., 2018) were also assigned a confidence score of 3. Conversely, reactions not associated with the selected expressed genes were assigned a confidence score of  $-1$ , reflecting low confidence due to presumed lack of expression. After reconstructing draft GSMMs from all five thresholds for each sample, the models from all timepoints were merged to create a comprehensive, context-specific GSMM representative of HEK293 cells. This “adapted” CORDA approach was compared to the default method (Schultz and Qutub, 2016), which involved assigning confidence scores ranging from  $-1$  to  $3$  to reactions based on gene expression levels. Validation was conducted by integrating provided exchange rates calculated from the same samples (Dietmair et al., 2012) and predicting growth rates with flux balance analysis (FBA), using Cobrapy (v 0.22.1). The predicted growth rates were compared to experimental growth rates (Dietmair et al., 2012) and to predicted growth rates from the same process using a manually curated GSMM (Quek et al., 2014), based on Recon2 (Swainston et al., 2016).

Next, we analyzed two strains (LP and HP) under two distinct experimental conditions (mock and transfected) across five timepoints (0, 4, 24, 48, and 72 HPT). Each combination of strain, condition, and timepoint was evaluated in four biological replicates, resulting in a total of 80 transcriptomic samples. Using these transcriptomic datasets (Pistek et al., 2023), we applied five distinct thresholds — representing the top 10%, 25%, 50%, 75%, and 90% of expressed genes for draft-GSMM construction. This resulted in 320 individual GSMMs. To facilitate downstream comparative analyses and enhance biological interpretability, we integrated the models generated for each combination of timepoint, condition, and strain. This process resulted in 16 comprehensive, context-specific GSMMs for two strains (LP and HP), two conditions (mock and transfected), at five timepoints (0, 4, 24, 48, 72 HPT). During the subsequent optimization of production reactions, it was noted that the transport reactions of three nucleotides from the cytoplasm into the nucleus were not included in the models and were therefore added manually. To validate the reconstruction, we employed two approaches: first, we applied LPCA (Landgraf and Lee, 2020) to the differential reaction set (Zehetner et al., 2024) of all models and compared the results to those obtained from PCA applied to transcriptomes as shown in Pistek et al. (2023). For all simulation

related analyses, we used only models from four timepoints (4, 24, 48, 72 HPT), since a medium exchange was performed before transfection, which did not allow us to include metabolite concentrations from timepoint 0. Secondly, we integrated the calculated exchange rates and obtained simulated growth rates using FBA, where the lower bound ( $lb_i$ ), and upper bound ( $ub_i$ ) for each metabolite  $i$  was calculated by:

$$lb_i = q_i - q_{err,i} \quad (13)$$

$$ub_i = q_i + q_{err,i} \quad (14)$$

These simulated growth rates were then compared to experimentally determined growth rates. Production reactions for AAV were incorporated into the models using Biopython (v1.79) and AAV genomes (NCBI UID: 5075992). After integrating the production reactions into the models, we analyzed the production envelope at each timepoint and performed comparative analyses between the cell lines.

### 2.3.5. Calculation of specific production rate from experimental titers

First, production reactions for AAV production were added. The viral genome from AAV 8 was downloaded and the sequence for viral proteins VP1, VP2, and VP3 was extracted. The ratio of 1:1:10 (VP1:VP2:VP3) was considered in the production reaction (Samulski and Muzyczka, 2014). Additionally, the replicated genome was considered as 4.8 kb long and consisting of 25% Adenine, 25% Guanine, 25% Thymine, and 25% Cytosine. Moreover, we added transport reactions for all amino acids into the nucleus, since AAV production occurs in the nucleus (Nguyen et al., 2021)

- Production of VP1 in the nucleus
- Production of VP2 in the nucleus
- Production of VP3 in the nucleus
- Assembly of a full capsid with ratio 1:1:10
- Production of transgene
- Assembly of full capsids
- Transport of full capsids from nucleus into the cytoplasm
- Transport of full capsid from cytoplasm outside of the cell
- Exchange reaction for full capsid

See supplemental material for a detailed explanation of the added reactions for AAV production. Additionally, we added transport reactions of amino acids to the nucleus, since AAV replication happens in the nucleus (Nguyen et al., 2021).

We calculated specific production rates from experimental data. Experimentally, titers could only be determined at 24, 48, and 72 HPT, as the productivity at 4 HPT was too low to measure accurately. Consequently, we calculated the percentage of biomass allocated to production at 24, 48, and 72 HPT to minimize discrepancies with the experimentally determined titers. This was done by setting the lower bound ( $lb$ ) of the biomass reaction to the maximum growth rate, multiplied by a specific value  $\alpha_t$  for each strain and time point.

$$lb_t = \alpha_t \cdot \mu_{max,t} \quad (15)$$

After that,  $\alpha$  was determined by optimizing the production reaction, so that the squared difference between the simulated production rate and the experimental production rate is minimal. For optimization, we used a differential\_evolution algorithm from scipy (v 1.7.3) with bounds between 0, and 1, since the  $\alpha$  values should describe a percentage of the maximal biomass, that is used for production of AAV. We used the best1bin strategy with a maximum of 10 iterations, a population size of 15, and a tolerance of  $10 \cdot 10^{-7}$ . Using these factors ( $\alpha$ ), and assuming that at time point 0 HPT, all resources are directed towards growth giving an  $\alpha$  value of 1, we predicted an  $\alpha$  value at 4 HPT using a weighted mean, following:

$$\alpha_4 = \frac{\sum_i w_i \alpha_i}{\sum_i w_i} \quad (16)$$

with

$$w_i = \frac{1}{|t_i - 4|}, \quad (17)$$

where  $w_i$  are the factors to weigh the impact on the  $\alpha_i$  values from timepoints  $t_i$ , considering 0, 24, 48, and 72 HPT. This predicted  $\alpha$  value was then used to calculate the specific production rate in the GSMMs at 4 HPT. After determining all production rates, we generated a realistic production envelope to compare the two cell lines by fixing simulated growth rates and maximizing production rates. Additionally, we determined ideal production rates, by decreasing the simulated growth rate percentually from 1 to 0.7 and optimized the production rate at every timepoint, and for both strains.

### 2.3.6. Loopless flux sampling for differential reaction analysis

For analysis of GSMMs between cell lines, we conducted loopless flux sampling. First, we fixed the calculated growth and production rates to the obtained values and used the function `loopless_solution` to generate 1000 flux samples per GSMM using the `OptGPSampler` with default settings in `cobrapy` (Megchelenbrink et al., 2014). In case a GSMM could not be sampled due to numerical issues, we relaxed the biomass constraints by 5%. Next, we used the function `calculate_loopless_fluxes` in `cobrapy` to correct all flux samples for loops (Desouki et al., 2015). The loopless flux samples were then used to train a random forest classifier (Pedregosa et al., 2011). Loopless flux samples from all conditions at one time point were first merged into one dataset, followed by converting them into Dask DataFrames (Rocklin, 2015). Each dataset was subsequently used to build a random forest classifier by splitting it into training and test subsets (80/20 ratio) using Dask's train-test split function, ensuring random shuffling. Subsequently, reaction (feature) scaling was performed using a `StandardScaler` to normalize the data. Hyperparameter optimization was conducted via `RandomizedSearchCV`, leveraging a wide parameter grid and ROC-AUC as the scoring metric, to identify the optimal model configuration. The final model was validated using stratified k-fold cross-validation (five splits) to account for class imbalance, with performance assessed through ROC-AUC scores. The optimized model was then evaluated on the test set, and classification performance metrics were recorded.

To analyze the underlying features for GSMM separation, SHAP (SHapley Additive exPlanations) analysis was employed to interpret feature importance (Lundberg, 2017). SHAP values were computed for the test set to assess contributions of individual features across various conditions. SHAP values for each feature were aggregated and compared across conditions within each time point using the Kruskal-Wallis test (`scipy` v1.14.1 (Virtanen et al., 2020)). Multiple testing correction was applied using the Benjamini-Hochberg procedure using the `statsmodels` package (v0.14.4) (Sebold and Perktold, 2010), identifying significant features with adjusted p-values < 0.05. We discussed those reactions, that were identified to be significantly different across all four time points or across the first three time points (4, 24, 48 HPT).

### 2.4. Differential gene expression analysis of selected genes

Genes assigned to reactions from the above analysis were extracted, and analyzed using a t-test (`scipy`, v1.14.1) (Virtanen et al., 2020) with Benjamini-Hochberg correction for multiple testing (`statsmodels` v0.14.4) (Sebold and Perktold, 2010). We compared expression of HP and LP samples (Pistek et al., 2023) combining all timepoints and conditions. Genes with differential expression (adjusted p-value < 0.05) were extracted and further discussed.

### 2.5. Fermentation for validation

Six validation experiments were conducted: two vessels with the original AAV production process, two vessels with added limiting amino acids, and two vessels with a HIF-1 $\alpha$  inhibitor. We used 1 mg of the HIF-1 $\alpha$  inhibitor PX-478 dihydrochloride (Merck KGaA, Darmstadt, Germany), dissolved in 1 mL F17 media per 250 mL of fermentation suspension. For the vessels with added limiting amino acids, aspartate, and glutamate (Merck KGaA, Darmstadt, Germany) were added at 1.5 times the initial amount (0 HPT). Control settings were used as described before (see section Bioprocess and Sampling).

## 3. Results and discussion

### 3.1. HP cells are larger but lighter than LP cells

The dry cell mass and the composition of biomass – including total proteins, lipids, DNA, RNA, and carbohydrates – were quantified at five time points during fermentation for both the HP and LP strains. In both strains, transfection had no influence on total mass or composition. However, the dry mass decreased over time, with the LP strain showing a steeper decline.

As shown in Fig. 2(a), the dry mass of the HP strain ranged from 295 pg/cell to 380 pg/cell, with an average of 339.2 pg/cell, demonstrating more consistency over time compared to the LP strain, which ranged from 298 pg/cell to 447 pg/cell, averaging 388.9 pg/cell (adj. p-value  $6.515 \cdot 10^{-4}$ , t-test, Bonferroni correction).

For both strains, this was lower than the previously reported 514 pg/cell (Dietmair et al., 2012; Quek et al., 2014). However, this difference may be attributed to variations in cell composition, as the data in Quek et al. (2014) were derived from multiple human cell lines based on Recon2 (Thiele et al., 2013). In comparison, the average biomass for CHO cells is 264 pg/cell (Szélliová et al., 2020), making the dry mass in our study generally higher.

The relative composition analysis showed that the contributions of lipids, DNA, and RNA remained almost constant over time and were independent of the strain (Fig. 2(b)). In contrast, the HP strain had a higher protein content compared to the LP strain, particularly during the first 4 HPT. Since the amounts of lipids, DNA, and RNA were similar in both strains, the higher protein content in the HP strain suggests that other components contributing to dry mass must be higher in the LP strain. In fact, 35% of the dry mass in the LP strain, especially early post-transfection, remains unaccounted for. A similar high proportion of unknown dry mass has also been observed in some CHO cells (Szélliová et al., 2020). These authors suggested that ions, polyamines, and other small molecules likely make up much of the unaccounted biomass. Differences in the unexplained fraction between the HP and LP strains may reflect strain-specific metabolic adaptations, which could also influence experimental outcomes. For example, variations in lipid composition might alter cell membrane fluidity (Van Meer et al., 2008; Meer and Kroon, 2011), affecting cellular responses to shear stress and potentially impacting procedures such as sampling, cell counting, or lysis.

The HP strain displayed a higher volume regardless of the production state of the strain, despite having a lower dry mass compared to the LP strain (Fig. 2(c)).

### 3.2. HP Stores energy as triacylglyceride; LP prefers glycogen

Next, we investigate the lipid profile for both strains that on average represented approximately 10% to 18% of the total biomass irrespective of the strain. We observed that phosphatidylcholine (PC) and phosphatidylethanolamine (PE) dominated across all time points (Fig. 3(b)) accounting for about 65% of the total lipids and reflecting their essential role in mammalian cell membranes (Cockcroft, 2021; Tsuji et al., 2021). Our distribution aligns with previous analyses of

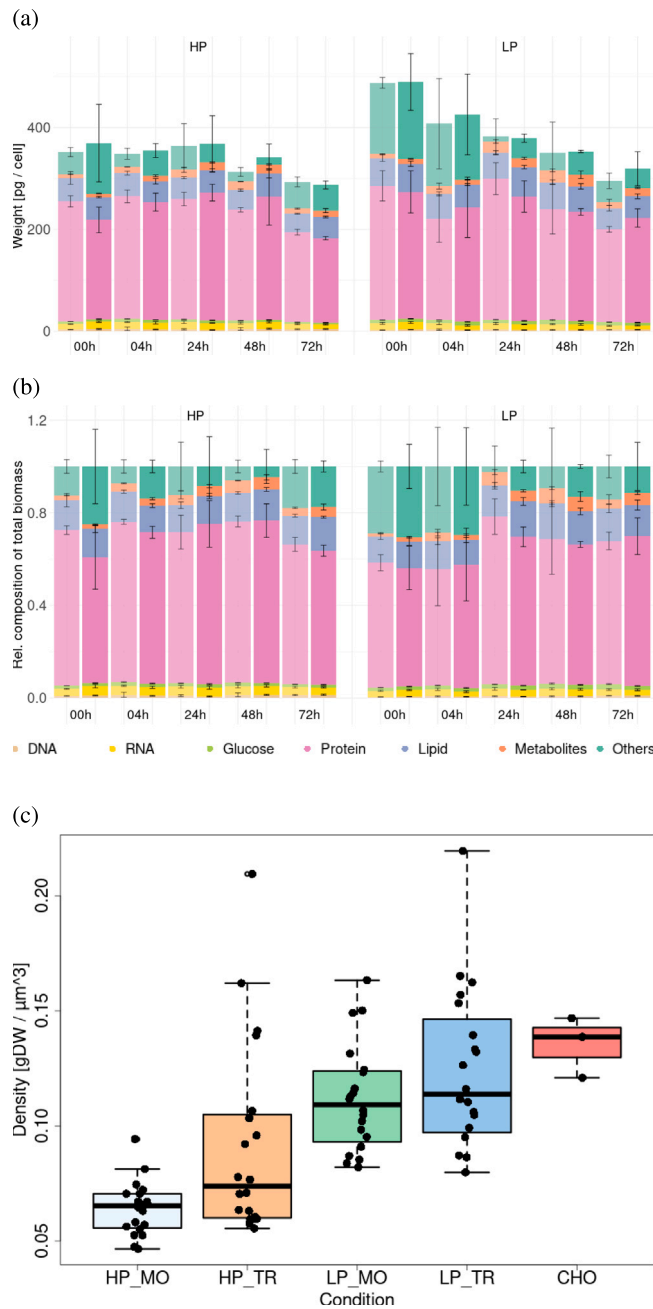


**Fig. 2.** Absolute (a) and relative (b) biomass composition, and volumetric mass density (c) for HP and LP strains. The LP had a higher dry mass (adjusted  $p = 6.515 \times 10^{-4}$ , t-test, Bonferroni correction) and density (adjusted  $p = 6.805 \times 10^{-7}$ , t-test, Bonferroni correction), but a smaller volume (adjusted  $p = 8.637 \times 10^{-7}$ , t-test, Bonferroni correction) compared to the HP. In the first 4h, the HP had a higher relative protein content, while other components were similar between strains. Transfected states are displayed fully colored, while mock states are transparent. We added default metabolite data from the human1 GSMM (Robinson et al., 2020).

HEK293 strains during exponential and stationary phases (Zhang et al., 2017) and mirrors typical mammalian cell lipid profiles (Vance, 2008, 2015).

PCA analysis clearly distinguishes between HP and LP, regardless of whether the cells were mock-transfected or transfected (Fig. 3(a)). This separation is mainly driven by differences in triacylglycerides (TG), ceramide (Cer), phosphatidylethanolamine (PE), and phosphatidylglycerols (PG). HP cells show higher levels of TG and Cer but lower levels of PE and PG compared to LP. These lipid concentrations also change over

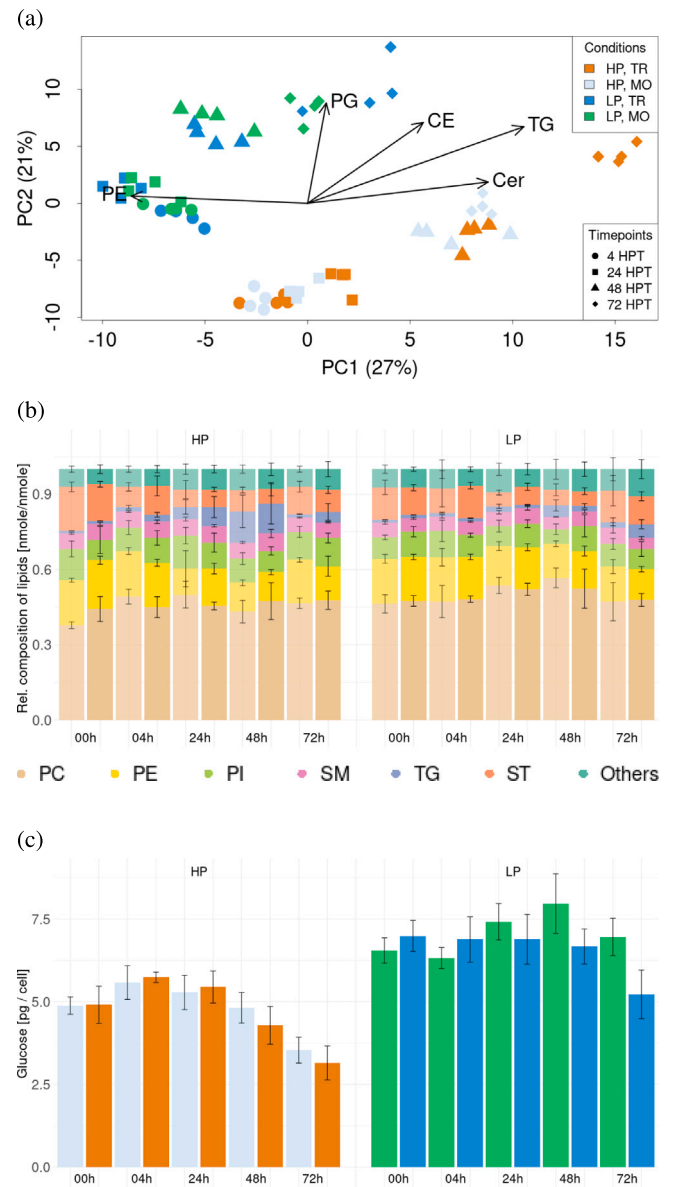


**Fig. 3.** PCA of lipid profiles (a), relative lipid (b), and glucose (c) composition of HEK293 strains during AAV production and mock states. PCA resulted in a clear separation of HP and LP (a), with the five most influential lipid groups highlighted by their loadings. The predominant drivers for the separation of the strains were TG, and Cer, pinpointing in the direction of the HP cluster, while PE and PG loading vectors directed in the LP cluster. PE, PI, and PC constitute the majority of lipids in both, HP and LP strains. TG amounts changed most significantly from 1% to 12% in the HP strain until 48 HPT, indicating that the HP stored glucose as TG (b), while the LP stored glucose predominantly as glucogen (c).

time, with TG and Cer increasing as fermentation progresses, while PE decreases (Fig S1). In the HP strain, phospholipid levels ranged from 5% to 12% (Cer), 7% to 13% (PG), and 10% to 19% (PE), whereas in the LP strain, they ranged from 4% to 10% (Cer), 7% to 18% (PG), and 12% to 18% (PE).

The greatest difference was observed in TG levels, which rose from 1% to 12% in HP during the first 48 h, compared to only 1% to 5% in LP. This suggests distinct lipid storage strategies between the two strains.

An increase in lipid storage and cell volume was also observed in antibody-producing CHO cells (Pan et al., 2017). This was linked to fatty acid synthesis exceeding the demand for membrane lipid production, potentially due to the lower surface-to-volume ratio in larger cells.

**Table 2**

Comparison of the number of reactions in HEK293F-specific GSMMs and their predicted growth rates ( $\mu$ ) with the measured exponential growth rate ( $\mu_{ref}$ ) as reported in Dietmair et al. (2012). ‘Default’ and ‘adapted’ CORDA (Schultz and Qutub, 2016) refer to the models developed in this study (see methods); (Quek et al., 2014) represents a previously established model. The relative error  $\Delta\mu$  is defined as  $\mu/\mu_{ref} - 1$ .

Experimental growth rate (Dietmair et al., 2012) $\mu_{ref} = 0.0281 \text{ h}^{-1}$			
	Quek et al. (2014)	CORDA	
		default	adapted
Reactions	357	5318	7740
Genes	–	2659	3035
Metabolites	–	3950	5015
$\mu$ [ $\text{h}^{-1}$ ]	0.0213	0.0121	0.0301
$\Delta\mu$ [%]	–24.2	–56.9	7.1

Interestingly, the LP appeared to store glucose mainly as glycogen, as indicated by its higher glucose content relative to HP (Fig. 3(c)). This suggests a potential metabolic bottleneck in LP, possibly due to oxygen limitation (see below), since glycogen is a less efficient form of energy storage compared to fatty acids (Batchuluun et al., 2022). Additionally, HP cells displayed more dynamic changes in storage capabilities over time compared to LP, further highlighting differences in energy storage strategies between the strains.

Cholesterol esters (CE) increased similarly in both strains, correlating with the progression of fermentation rather than distinguishing between them.

Finally, we speculate that lipid remodeling occurs following transfection, characterized by an initial increase in short-chain fatty acids shortly after transfection, with the lipid profile gradually returning to its original distribution by the end of fermentation (Fig. 3(b)). However, this effect is less pronounced and appears less evident in the LP strain.

### 3.3. GSMMs Capture transcriptomic and growth trends

To further investigate the metabolic differences between HP and LP, we reconstructed strain-specific GSMMs using CORDA (Schultz and Qutub, 2016); see Methods for details. These models are based on the integration of the biomass composition (reported above), together with transcriptome and exometabolome measurements collected throughout the fermentation process.

To validate our reconstruction pipeline, we used transcriptomic data and exchange rates from independent studies (Dietmair et al., 2012; Quek et al., 2014) to build a strain-specific GSMM for a non-producing HEK293F strain. The model predicts a specific growth rate of  $0.0301 \text{ h}^{-1}$ , which closely matches the experimentally measured rate of  $0.0281 \text{ h}^{-1}$ , resulting in a relative error of 7.1% (Table 2). This solid agreement indicates a good accuracy of our model and validates our reconstruction approach.

Next, we reconstructed 80 context-specific GSMMs for each of the four replicates of our two producer strains at five time points, using transcriptomic data from Pistek et al. (2023), and the corresponding media composition. To assess whether these models captured the differential information present in the transcriptome (Fig. 4(a)), we collected model metrics (Table 3), and applied LPCA (Zehetner et al., 2024), a method we previously demonstrated to replicate clustering patterns observed in transcriptome-based PCA using only GSMMs. As expected, LPCA of the reconstructed metabolic models revealed clustering patterns similar to those from transcriptome-based PCA (compare Fig. 4(a) with Fig. 4(b)). These findings suggest that even at the metabolic level strain differences were more pronounced than between conditions or time points.

Finally, to assess the quality of our context-specific GSMMs for both producer strains, we used FBA to simulate growth rates over 4 HPT to 72 HPT, using the measured exchange spectrum as input, and compared the results to a logistic fit of the experimentally measured

**Table 3**

Comparison of Reactions, Genes, and Metabolites in HEK293-specific GSMMs. Numbers were extracted at four time points (4HPT to 72 HPT) for MO and TR. Values represent minima and maxima across all time points and conditions.

	HP	LP
Reactions	9074–9188	8993–9155
Genes	3109–3117	3109–3116
Metabolites	6196–6245	6189–6243

growth curve. We observed reasonable agreement ( $\pm 25\%$ ) at intermediate growth rates, while lower rates were overestimated (Fig. 4(c)). For higher growth rates, the large deviations were possibly due to reduced reliability in the experimental data, as indicated by substantial error bars. Nevertheless, the error bars of most experimental data points at least intersect with the  $\pm 25\%$  region around our predictions (Fig. 4(c)), supporting the overall robustness of our model predictions.

### 3.4. HEK293 strains differ in limiting compounds in spent media

In addition to biomass analyses, we performed a spent media analysis as described in the methods. We identified the amino acids aspartic acid, and glutamic acid in the LP strain and serine in the HP strain as limiting, regardless of the state (see Fig S2 d, Fig S3 a, and Fig S4 d).

### 3.5. HEK293 strains have similar AAV production potential, but drastically lower actual rates

After integrating AAV particle production reactions into the GSMMs of the HP and LP strains (see Supplementals), we applied FBA to compute production envelopes at four time points ranging from 4 to 72 HPT (Fig. 5). These envelopes represent the maximum production capacity of each strain as a function of growth rate. We found that, for the experimentally measured uptake rates, both strains exhibit nearly identical production capabilities. This means that despite the differences in their GSMMs, the overall production potential of HP and LP is stoichiometrically almost the same. However, while the actual production rate in HP is up to six times higher than in LP, both strains produce at rates that are two orders of magnitude lower than their theoretical maximum production capacity.

### 3.6. Keto-body secretion differentiates HP from LP strains

To understand why the LP strain underperformed compared to the HP strain, we performed flux sampling for both TR and MO conditions. Significant differences in individual reaction fluxes were identified using a random forest classifier with SHAP value analysis and Kruskal–Wallis tests applied to loopless flux samples. At each time point, the random forest classifier achieved an ROC-AUC score of 1.0, along with perfect precision and recall scores. This demonstrates the classifier’s reliability in distinguishing conditions and its robustness in identifying reactions of interest.

We identified eleven reactions with significant flux differences over at least the first three time points (4, 24, and 48 HPT). Of these, four were associated with specific genes, and five were exchange reactions. Subsystems (derived from human1 (Robinson et al., 2020)) and cellular locations were assigned where possible to provide insights into potential enrichments and functional roles (Table 4).

Six of the eleven reactions exhibited higher flux in LP, while five showed higher flux in HP. Notably, four of the five higher-flux reactions in HP were exchange reactions. Among these, two – glutamine (MAR09063) and glutamate (MAR09071) – were experimentally measured, while pantothenate uptake (MAR09145), an essential minimal media component, was fully coupled to the biomass reaction. The remaining exchange reactions were beta-hydroxybutyrate (BHB) (MAR09134) and acetoacetate (MAR09132).

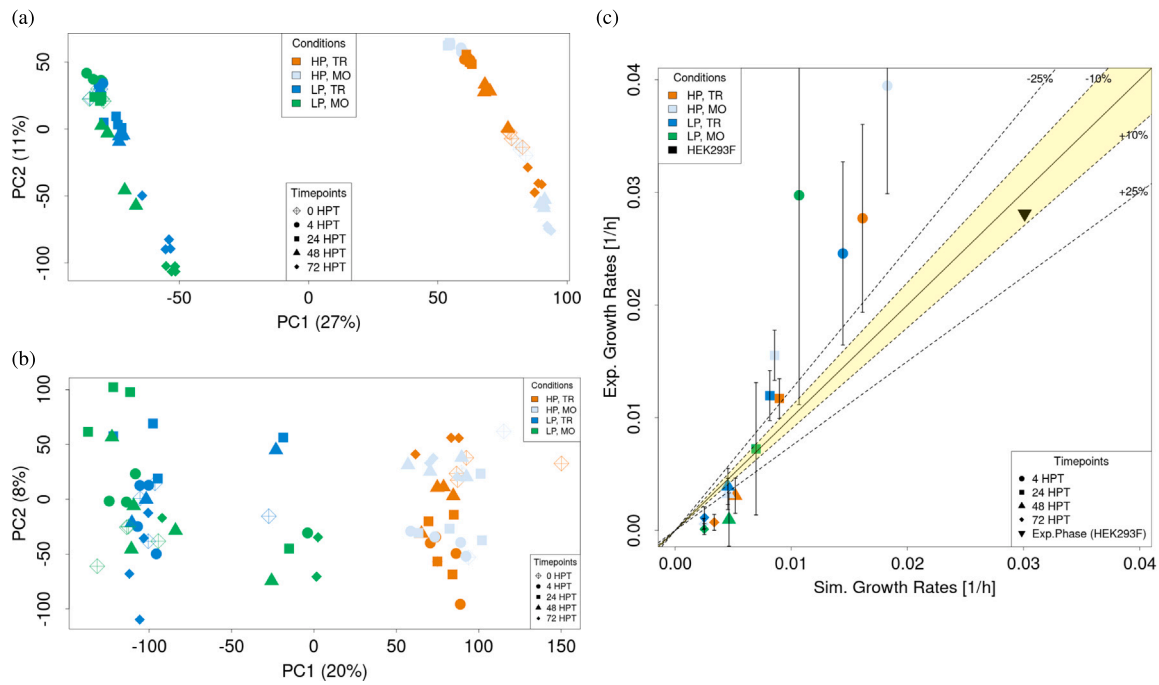


**Fig. 4.** PCA from transcriptomic data (a), LPCA of binary reactions matrix derived from GSMMs (b), and simulated vs. experimental growth rates (c). When comparing LPCA (b) with a PCA plot performed on whole transcriptomes (a) we observed a similar clustering, indicating that GSMMs capture differences between strains in a similar way. Growth rates were calculated from dry mass measurements. Error bars were obtained after fitting the regression function (see methods). Simulated growth rates were obtained after merging biological replicates. Aside from the first time points 4 HPT, the simulated and experimental growth rates are comparable, indicating that the GSMMs can capture realistic growth rates during AAV production and in mock state (c).

**Table 4**

Comparison of reactions with consistently higher (red) or lower (blue) fluxes in the GSMMs of LP vs. HP over the first three time points (4 HPT to 48 HPT). Each reaction is listed with its gene–protein–reaction (GPR) mapping, where overexpressed genes are in red and underexpressed genes in blue. Biochemical functions and metabolic subsystems are also included. Bold genes indicate regulatory targets of HIF-1 $\alpha$  (see main text).

Reaction ID	Gene-Reaction Rule	Subsystem	Cellular localization
MAR09063	–	Exchange reactions	Extracellular
MAR09071	–	Exchange reactions	Extracellular
MAR09132	–	Exchange reactions	Extracellular
MAR09134	–	Exchange reactions	Extracellular
MAR09145	–	Exchange reactions	Extracellular
MAR02421	<b>TECR</b> or <b>TECRL</b>	Omega-6 fatty acid metabolism	Cytosol
MAR02307	<b>HSD17B12</b>	Fatty acid biosynthesis (unsaturated)	Cytosol
MAR02343	<b>HSD17B12</b>	Fatty acid biosynthesis (unsaturated)	Cytosol
MAR02229	<b>FASN</b>	Fatty acid biosynthesis (odd-chain)	Cytosol
MAR10365	–	Transport reactions	Cytosol
MAR06902	–	Transport reactions	Mitochondria

### 3.7. Absence of BHB secretion links to HIF-1 $\alpha$ activity in LP strain

Acetoacetate secretion was consistently upregulated in the LP strain across the first three time points, whereas BHB secretion was not only higher in the HP strain but entirely absent in the LP strain reconstructions. Of the 320 draft GSMMs (two strains, two conditions, four time points, four biological replicates, five gene expression thresholds), which resulted in 16 GSMMs per condition used for simulation, none of the LP models included the exchange reaction for BHB, while all HP models enabled BHB secretion. The complete absence of BHB secretion in LP models highlights a critical metabolic divergence between both strains.

BHB exhibits protective effects against oxidative stress (Newman and Verdin, 2014) and possesses anti-inflammatory properties (Qi et al., 2022). This corresponds with previous transcriptomic analyses of our cell lines, which revealed heightened inflammatory activity in the LP strain compared to the HP strain, irrespective of transfection status (Pis-tek et al., 2023; Kahlig et al., 2024). Moreover, BHB has been shown to

inhibit a key transcription factor HIF-1 $\alpha$  (Ma et al., 2022). BHB treatment reduces HIF-1 $\alpha$  activity under hypoxic conditions, particularly at high concentrations. This effect occurs post-translationally, as BHB does not alter HIF-1 $\alpha$  mRNA levels (Ma et al., 2022).

### 3.8. HIF-1 $\alpha$ activation significantly impairs cellular metabolism

HIF-1 $\alpha$  upregulates glycolytic enzymes and glucose transporters, enhancing glucose uptake and catabolism while suppressing tricarboxylic acid (TCA) cycle activity (Wang et al., 2017; Corcoran et al., 2016). A key mechanism in the suppression of the TCA is the HIF-1 $\alpha$ -mediated upregulation of pyruvate dehydrogenase kinase (PDK), which inhibits pyruvate dehydrogenase, reducing pyruvate entry into the TCA cycle (Kim et al., 2006). Consequently, cells may utilize glutamine or glutamate as alternative carbon sources (Frezza et al., 2011). This metabolic shift leads to the accumulation of TCA cycle intermediates, notably succinate, and fumarate, which further activate HIF-1 $\alpha$  by inhibiting its regulator, prolyl hydroxylase (PHD) (Semenza, 2003).

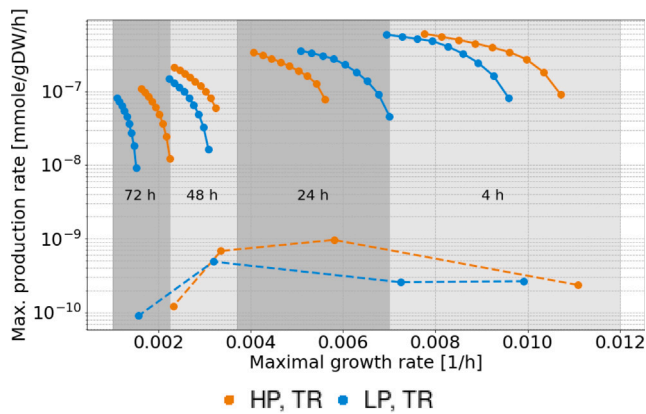


**Fig. 5.** Production envelope of HEK293 strains (HP: orange, LP: blue) 4 HPT, 24 HPT, 48 HPT, 72 HPT (solid lines), as well as the real production envelope (dashed line). For every time point and cell line, the maximum growth rate was determined by FBA. These maximum growth rates were then fractionally reduced to 70% and fixed to the  $lb_{hm}$ , before optimizing for AAV production. The resulting solid lines displayed at the top of the plot represent the maximum production capacity. The production envelope based on experimental data (dashed line) was obtained after calculating the fraction of biomass, used for production. While the experimental production rate of the HP strain is higher compared to the LP strain, both strains are two orders of magnitude lower than their theoretical maximum production rate.

Indeed, transcriptomic data showed significant upregulation of HIF-1 $\alpha$  in the LP strain (adj.  $p$ -value  $3.239047 \times 10^{-17}$ , t-test, Bonferroni correction), as well as HIF-1 $\alpha$ -regulated *PDK* (adj.  $p$ -values: *PDK1*: not significant, *PDK2*:  $4.802597 \times 10^{-16}$ , *PDK3*:  $1.343645 \times 10^{-12}$ , *PDK4*:  $9.975931 \times 10^{-16}$ , t-test, Bonferroni correction). Given the substantial post-translational regulation of HIF-1 $\alpha$  by PHD, we sought additional evidence of its activation within the GSMMS.

### 3.8.1. Results from GSMMS support hypothesis of HIF-1 $\alpha$ to be activated in the LP strain

While both strains exhibited glutamine uptake, the LP strain displayed a significantly higher uptake rate across all time points (4, 24, 48 HPT). The HP strain secreted glutamate, while the LP strain consistently took it up at all time points (see spent media profiles Fig S3 a, Fig S2 g). Both amino acids are involved in glutaminolysis, a pathway upregulated in cells with activated HIF-1 $\alpha$  to generate ATP (Kappler et al., 2019). Glutaminolysis converts glutamine to glutamate, which is then transformed into alpha-Ketoglutarate (AKG) to enter the TCA cycle. Gene expression analysis revealed significant upregulation of all glutaminolysis-related genes in the LP strain (adj.  $p$ -values: *GLUD1*:  $1.232318 \cdot 10^{-05}$ , *GLUD2*:  $2.74860 \cdot 10^{-05}$ , *GLUL*:  $6.402998 \cdot 10^{-05}$ , t-test, Bonferroni correction). However, it remains unclear whether increased glutaminolysis drives HIF-1 $\alpha$  activation or whether HIF-1 $\alpha$  activation induces elevated expression of glutaminolysis-related genes in the LP strain.

To investigate further, we examined which downstream TCA metabolites of AKG might accumulate in cells by analyzing sampled fluxes of secretion reactions in the GSMMS at the first two time points. Notably, fumarate secretion was significantly higher in the LP GSMMS at 4 and 24 HPT. Indeed, excessive fumarate accumulation inhibits succinate dehydrogenase (SDH), a key component of the mitochondrial electron transport chain (ETC). SDH inhibition blocks electron transfer from succinate to ubiquinone, disrupting electron flow through the ETC (Tyrakis et al., 2017). This reduces NADH oxidation at complex I, causing NADH accumulation as it cannot efficiently convert back to NAD (Rustin et al., 2002). Impaired electron flow decreases the proton gradient across the inner mitochondrial membrane, reducing ATP production via oxidative phosphorylation (Mills et al., 2016). This may impair viral DNA replication, since the viral Rep68 is an

ATP-dependent endonuclease with helicase activity (Im and Muzyczka, 1990).

Further analysis revealed that the gene encoding fumarate hydratase, which converts fumarate to malate, was significantly upregulated in the HP strain (adj.  $p$ -value  $5.363976 \cdot 10^{-19}$ , t-test, Bonferroni correction). This could potentially explain the accumulation of fumarate in the LP strain. Elevated fumarate levels have been identified as a potent factor for HIF-1 $\alpha$  stabilization and activation, creating a positive feedback loop (Shanmugasundaram et al., 2014; Ooi and Furge, 2012; Yang et al., 2012).

HIF-1 $\alpha$  activation as well as fumarate accumulation have been associated with increased glucose uptake (Yang et al., 2013) and aerobic glycolysis (Frezza et al., 2011). On the other hand, high fumarate levels have also been linked to reduced glycolysis in macrophages (Jeridi et al., 2023). While both LP and HP exhibited aerobic glycolysis, we found similar glucose uptake rates between the LP and HP strains. However, the LP strain stores higher amounts of glucose as glycogen (Fig. 3(c)), while the HP strain generates higher levels of lactate (Fig S3 e), and stores excessive glucose as triacylglycerides (Fig. 3(b)). The higher lactate secretion aligns with the amount of base required to maintain stable pH in the bioreactor: the HP strain necessitated greater base addition during the culture period (18.39–21.21 mL over 72 HPT) compared to the LP strain (11.14–13.26 mL over 72 HPT), despite no significant differential expression of *LDH*.

HIF-1 $\alpha$  is typically activated under oxygen deprivation (Chun et al., 2002). However, in bioreactors with constant and monitored oxygen supply, HIF-1 $\alpha$  activation may result from elevated reactive oxygen species (ROS) levels or mitochondrial dysfunction (Zeidan et al., 2022; Liang et al., 2022; Chen et al., 2018). When analyzing gene expression values of ROS detoxifying enzymes like *SOD*-family genes, we observed a higher expression in the LP strain, compared to the HP strain (adj.  $p$ -values: *SOD1*: not significant, *SOD2*:  $1.974203 \cdot 10^{-20}$ , *SOD3*:  $1.938036 \cdot 10^{-05}$ ). High expression of *SOD* genes could indicate an adaption to increased oxidative stress, and therefore elevated ROS levels (Leone et al., 2017). These high ROS concentrations could be a potential reason for HIF-1 $\alpha$  activation in the LP strain. Despite these findings, the precise cause of HIF-1 $\alpha$  stabilization remains unknown. However, we hypothesize that HIF-1 $\alpha$  is activated in the LP strain but is either too low expressed or inactive in the HP strain, possibly due to extensive adaptation to suspension growth.

Beyond exchange reactions, we identified four reactions with significant differential flux associated with lipid metabolism as displayed in Table 4. Two of these reactions are catalyzed by the gene *HSD17B12* (adj.  $p$ -value  $3.441411 \cdot 10^{-16}$ , t-test, Bonferroni correction), one by *FASN* (adj.  $p$ -value  $4.304141 \cdot 10^{-12}$ , t-test, Bonferroni correction), and the fourth by *TECR* (adj.  $p$ -value  $2.147250 \cdot 10^{-07}$ , t-test, Bonferroni correction), which showed higher expression in the HP strain. Evidence suggests that under hypoxic conditions, HIF-1 $\alpha$  activation stimulates the expression and activity of *FASN*, enhancing fatty acid synthesis. This metabolic shift is a critical cellular adaptation to low-oxygen environments, supporting survival and proliferation under stress (Ezzeddini et al., 2019). However, as two of the four reactions demonstrated higher flux despite contrasting gene expression, the significance of these findings remains inconclusive.

### 3.8.2. Enriched unfolded protein response (UPR), ER stress, and inflammatory pathways in the LP strain could be consequences of HIF-1 $\alpha$ activation

Our findings provide a new perspective on prior results (Kahlig et al., 2024; Pistek et al., 2023). While gene set enrichment analysis (GSEA) identified upregulation of ER stress and the unfolded protein response (UPR) in the LP strain without pinpointing the underlying cause, the accumulation of fumarate, potentially following HIF-1 $\alpha$  activation, offers a plausible explanation. Elevated fumarate levels can contribute to oxidative stress through the production of succinyl-CoA, resulting in sustained oxidative stress and, consequently, ER stress (Zheng et al.,

2015). This effect can also be exacerbated by high glucose exposure (Manuel et al., 2020). Additionally, fumarate can induce protein succination at cysteine residues, which directly triggers UPR, and ER stress (Giallongo et al., 2023). Moreover, previous analyses (Pistek et al., 2023) identified immune pathway activation, particularly upregulation of *STAT1*, in the LP strain. Interestingly, *STAT1* was already upregulated prior to transfection, as evidenced in their study, suggesting an alternative driver for its expression (Pistek et al., 2023). High fumarate levels have been linked to immune activation, including increased tumor necrosis factor expression and suppression of interleukin-10 (Hooftman et al., 2023). Another study demonstrated that fumarate induces mitochondrial DNA (mtDNA) release into the cytosol, triggering inflammatory pathways. This mtDNA release activates the cGAS-STING pathway, leading to the upregulation of interferon-stimulated genes. This pathway also involves phosphorylation of *TBK1* and *IRF3*, which are key components of the type I interferon signaling cascade and strongly associated with *STAT1* activation (Zecchini et al., 2023). This interplay is particularly intriguing because *STAT1* and HIF-1 $\alpha$  are known to counteract each other in cancer environments (Hiroi et al., 2009; Zhang et al., 2022c). However, in the LP strain, both are upregulated, presenting an unusual coexistence that warrants further investigation.

### 3.9. Experimental validation

Based on our hypothesis, we inhibited the transcription factor HIF-1 $\alpha$  using PX-478 dihydrochloride, a known HIF-1 $\alpha$  inhibitor (Welsh et al., 2004; Koh et al., 2008; Zhu et al., 2017; Schwartz et al., 2009; Xu et al., 2022). As expected, PX-478 completely inhibited cell growth in the LP strain, confirming its strong dependence on HIF-1 $\alpha$  (Fig. 6(a), light blue). In contrast, adding aspartic and glutamic acid (Fig. 6(a), dark red), identified as limiting compounds in the spent media, did not significantly impact cell growth compared to the control fermentation (Fig. 6(a), dark blue).

Next, we assessed productivity under these conditions by measuring viral capsid concentration (Fig. 6(b)) and viral genome concentration (Fig. 6(c)). Interestingly, inhibiting HIF-1 $\alpha$  nearly doubled per-cell capsid production compared to the control ( $p$ -value < 0.006727,  $t$ -test), but viral genome production decreased. The increased viral capsids might be due to a redirected resource allocation — since cell growth was stalled in the LP strain, available amino acids could be utilized for capsid production. The decline in viral genomes might be due to reduced activity in the PPP, which is tied to HIF-1 $\alpha$  and vital for nucleotide synthesis (Jiang et al., 2014; Jin and Zhou, 2019). Since AAV genome replication depends on human DNA replication and repair proteins (e.g., MCM, Polymerase delta) (Nash et al., 2008), inhibiting HIF-1 $\alpha$ , and subsequent decreased synthesis of nucleotides in the PPP, possibly lead to the reduced amount of viral genomes. Future experiments could consider supplying HEK293 cells with nucleosides during production phase to overcome the decreased PPP due to inhibition of HIF-1 $\alpha$ .

## 4. Conclusion

HEK293 strains are currently the most prominent platform for the production of AAV particles in gene therapy (Bulcha et al., 2021; Wang et al., 2024). Despite numerous advances in the past decades (Clement and Grieger, 2016; Strasser et al., 2021; Blessing et al., 2019), production titers remain insufficient to meet necessary demands (Nguyen et al., 2021). In this study, we present a comprehensive multi-omics analysis, encompassing transcriptomic, lipidomic, metabolomic, and fluxomic data, to investigate and compare two different HEK293 strains in both mock and AAV production states.

When comparing the HP HEK293 strain with the LP strain, we found that the most significant differences were between the strains

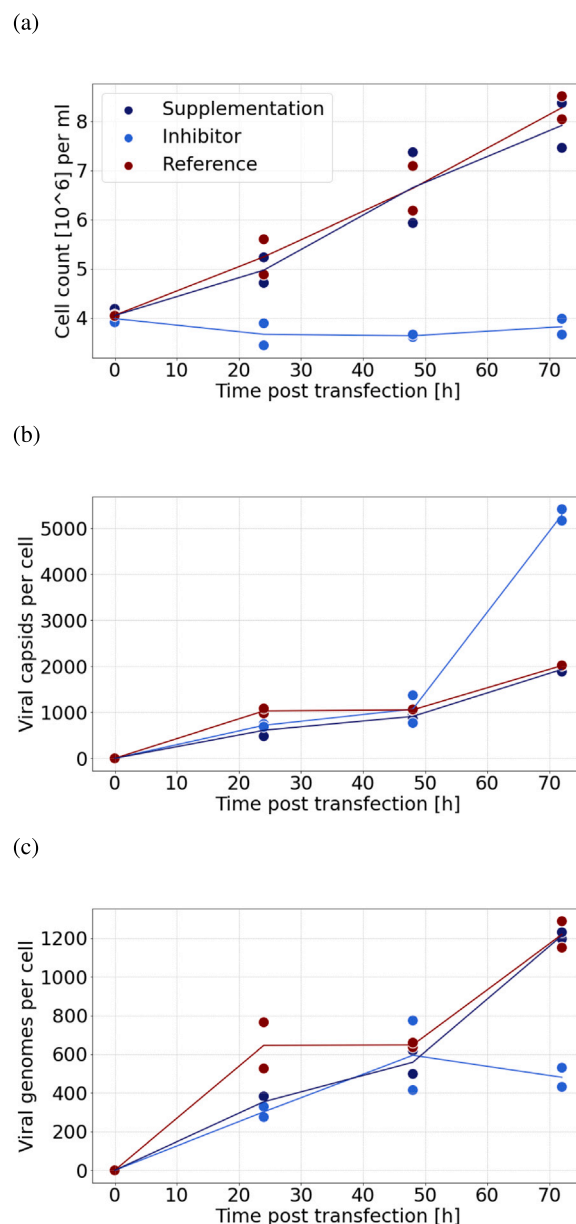


Fig. 6. Validation experiment, when inhibiting HIF-1 $\alpha$  in LP HEK293 strain during AAV production. HIF-1 $\alpha$  inhibition (light blue), showed halted growth (a), higher viral capsid production (b), but reduced viral genome production (c), while the production under original conditions (dark blue), and with aspartic acid, and glutamic acid supplemented (dark red), resulted in similar growth rates (a), and production rates (b, c).

themselves rather than between their production states, corroborating findings by Pistek et al. (2023). Recent studies on HEK293 cells have revealed high glucose consumption and elevated production of lactate and succinate (Jang et al., 2022), indicative of pseudohypoxia in HEK293 cells recently adapted to suspension culture. These observations were reproduced in subsequent studies during AAV production, which also showed upregulated immune responses (Pistek et al., 2023) and unfolded protein responses (Lu et al., 2024; Kahlig et al., 2024), without identifying the underlying cause. By employing a multi-omics approach and integrating GSMMs, we identified that the LP strain experiences activated HIF-1 $\alpha$ . Lipidomic analysis showed higher concentrations of ceramides in HP strains, indicating a tumor-like state in the LP strain. Exometabolomic analysis revealed that the LP strain preferentially consumes aspartate, glutamine, and glutamate, a common

behavior of solid tumor cells to maintain energy balance (Garcia-Bermudez et al., 2018). After identifying HIF-1 $\alpha$  as a potential target, we observed that it was significantly upregulated in the LP strain compared to the HP strain. This identification would have been more difficult in whole transcriptome analysis and Gene set enrichment analysis (GSEA) as performed by Kahlig et al. (2024), Pistek et al. (2023). Inhibiting HIF-1 $\alpha$  immediately halted cellular growth in the LP strain and doubled AAV capsid productivity. However, the number of viral genomes per cell decreased compared to standard production in the LP strain, likely due to insufficient nucleotide synthesis through the PPP. The PPP is central to synthesizing precursors for *de novo* nucleotide synthesis and is closely tied to HIF-1 $\alpha$  activity (Wang et al., 2017; Nagao et al., 2019; Corcoran et al., 2016) in hypoxic cells by directly regulating the essential PPP genes *TKT*, and *G6PD*, which catalyzes the rate limiting reaction in the PPP (Trejo-Solis et al., 2024; Tokuda et al., 2020). Inhibiting HIF-1 $\alpha$  likely downregulated *de novo* nucleotide synthesis, leading to fewer viral genomes. To mitigate this bottleneck, additional nucleotides could be supplemented in the media to maintain viral genome production. The overexpression of HIF-1 $\alpha$  has been exploited in bioprocesses involving CHO cells to enhance RP production. Specifically, the target gene was placed under the control of a HIF-1 $\alpha$ -responsive sequence, thereby ensuring that the RP is expressed upon HIF-1 $\alpha$  activation in CHO cells. This activation was achieved by inducing hypoxia through reduced oxygen flow (Zeh et al., 2021). These findings suggest that hypoxia and the activation of HIF-1 $\alpha$  may serve as critical regulators for bioprocess control and AAV production. Given that certain HEK293 strains may exhibit elevated fumarate levels, it is crucial to consider their potential impact on recombinant products, such as RP or AAV. Elevated fumarate levels can lead to succination of cysteine residues (Giallongo et al., 2023), potentially affecting proper protein folding or the assembly of AAV capsids by altering post-translational modifications. Succination of viral capsids has the potential to compromise the biopotency of AAV vectors. Biopotency of AAV refers to the specific ability of an AAV vector to deliver and express the intended transgene in target cells or tissues (Salmikangas et al., 2023). PTMs, such as phosphorylation, and glycosylation are commonly observed on AAV capsids and are critical for maintaining capsid stability, mediating cellular interactions, and facilitating intracellular trafficking (Mulcrone et al., 2023; Mary et al., 2019). Finally, the optimization of a GMP-conform bioprocess should not include any substances or additives, such as inhibitors, due to potential difficulties in downstream purification, which was not considered in this study. Therefore, it is necessary to create stable knockout strains, to inhibit the function of HIF-1 $\alpha$ , instead of using inhibitors, such as PX-478.

#### CRedit authorship contribution statement

**L. Zehetner:** Writing – review & editing, Writing – original draft, Visualization, Validation, Software, Methodology, Investigation, Formal analysis, Data curation, Conceptualization. **D. Szélliová:** Writing – review & editing, Supervision, Methodology, Conceptualization. **B. Kraus:** Writing – review & editing, Funding acquisition. **J.A. Hernandez Bort:** Writing – review & editing, Supervision, Project administration, Funding acquisition, Conceptualization. **J. Zanghellini:** Writing – review & editing, Supervision, Resources, Project administration, Conceptualization.

#### Code and data availability

All generated, and used data, as well as analyses are provided on GitHub: [github.com/LeoZ93/hek293aav](https://github.com/LeoZ93/hek293aav).

#### Declaration of competing interest

The authors declare that they have no known competing financial interests or personal relationships that could have appeared to influence the work reported in this paper.

#### Acknowledgments

The authors kindly thank the whole GTPD Upstream Team 1, specifically Manfred Ostermann, Katharina Portner, Ronald Leitner, Sonja Muellner, Robert Pachlinger, Susi Heider, Carolin Kahlig, and Lucia Micutkova, as well as Peter Andorfer, Peter Eisenhut, Bernd Innthaler, Felix Fuchsberger, Fabian Knofl, Andrea Seybel, Sabine Unterthurner, and Robert Pletzenauer for their support.

#### Appendix A. Supplementary data

Supplementary material related to this article can be found online at <https://doi.org/10.1016/j.ymben.2025.03.011>.

#### Data availability

All data generated and code used for analysis is available on Github

Improving HEK293-based AAV-production using GSMMs, and a multi-omics approach (Original data) (GitHub).

#### References

- Abaoudou, L., Quan, D., Shiloach, J., 2021. Affecting HEK293 cell growth and production performance by modifying the expression of specific genes. *Cells* 10, 1667.
- Agren, R., Bordel, S., Mardinoglu, A., Pornputtpong, N., Nookaew, I., Nielsen, J., 2012. Reconstruction of genome-scale active metabolic networks for 69 human cell types and 16 cancer types using INIT. *PLoS Comput. Biol.* 8, e1002518.
- Alazard-Dany, N., Nicolas, A., Ploquin, A., Strasser, R., Greco, A., Epstein, A., Fraefel, C., Salvetti, A., 2009. Definition of herpes simplex virus type 1 helper activities for Adeno-Associated Virus early replication events. *PLoS Pathog.* 5, e1000340.
- Aminian-Dehkordi, J., Mousavi, S., Jafari, A., Mijakovic, I., Marashi, S., 2019. Manually curated genome-scale reconstruction of the metabolic network of *Bacillus megaterium* DSM319. *Sci. Rep.* 9, 18762.
- Bairoch, A., 2018. The cellosaurus, a cell-line knowledge resource. *J. Biomol. Tech.: JBT* 29, 25.
- Batchuluun, B., Pinkosky, S., Steinberg, G., 2022. Lipogenesis inhibitors: therapeutic opportunities and challenges. *Nat. Rev. Drug Discov.* 21, 283–305.
- Becker, S., Palsson, B., 2008. Context-specific metabolic networks are consistent with experiments. *PLoS Comput. Biol.* 4, e1000082.
- Bernstein, D., Sulheim, S., Almaas, E., Segrè, D., 2021. Addressing uncertainty in genome-scale metabolic model reconstruction and analysis. *Genome Biol.* 22, 1–22.
- Blessing, D., Vachey, G., Pythoud, C., Rey, M., Padrun, V., Wurm, F., Schneider, B., Déglon, N., 2019. Scalable production of AAV vectors in orbitally shaken HEK293 cells. *Mol. Therapy- Methods & Clin. Dev.* 13, 14–26.
- Brunk, E., Sahoo, S., Zielinski, D., Altunkaya, A., Dräger, A., Mih, N., Gatto, F., Nilsson, A., Preciat Gonzalez, G., Aurich, M., et al., 2018. Recon3D enables a three-dimensional view of gene variation in human metabolism. *Nat. Biotechnol.* 36, 272–281.
- Buchsteiner, M., Quek, L., Gray, P., Nielsen, L., 2018. Improving culture performance and antibody production in CHO cell culture processes by reducing the Warburg effect. *Biotechnol. Bioeng.* 115, 2315–2327.
- Bulcha, J., Wang, Y., Ma, H., Tai, P., Gao, G., 2021. Viral vector platforms within the gene therapy landscape. *Signal Transduct. Target. Ther.* 6, 53.
- Castellano, B., Tang, D., Marsters, S., Lam, C., Liu, P., Rose, C., Sandoval, W., Ashkenazi, A., Snedecor, B., Misaghi, S., 2023. Activation of the PERK branch of the unfolded protein response during production reduces specific productivity in CHO cells via downregulation of PDGFR $\alpha$  and IRE1 $\alpha$  signaling. *Biotechnol. Prog.* 39, e3354.
- Catalan-Tatjer, D., Tzimou, K., Nielsen, L., Lavado-Garcia, J., 2024. Unravelling the essential elements for recombinant Adeno-Associated Virus (rAAV) production in animal cell-based platforms. *Biotechnol. Adv.* 108370.
- Chen, Y., Gustafsson, J., Tafur Rangel, A., Anton, M., Domenzain, I., Kittikunpong, C., Li, F., Yuan, L., Nielsen, J., Kerkhoven, E., 2024. Reconstruction, simulation and analysis of enzyme-constrained metabolic models using GECKO Toolbox 3.0. *Nat. Protoc.* 19, 629–667.
- Chen, R., Lai, U., Zhu, L., Singh, A., Ahmed, M., Forsyth, N., 2018. Reactive oxygen species formation in the brain at different oxygen levels: the role of hypoxia inducible factors. *Front. Cell Dev. Biol.* 6, 132.
- Chen, Y., McConnell, B., Gayatri Dhara, V., Mukesh Naik, H., Li, C., Antoniewicz, M., Betenbaugh, M., 2019. An unconventional uptake rate objective function approach enhances applicability of genome-scale models for mammalian cells. *NPJ Syst. Biol. Appl.* 5, 25.

- Chen, K., Wu, X., Yu, D., Ou, H., Li, Y., Zhou, Y., Li, L., 2018b. Process optimization for the rapid production of adenoviral vectors for clinical trials in a disposable bioreactor system. *Appl. Microbiol. Biotechnol.* 102, 6469–6477.
- Choi, Y., Choi, D., Lee, Y., Koduru, L., Lewis, N., Lakshmanan, M., Lee, D., 2023. Mitigating biomass composition uncertainties in flux balance analysis using ensemble representations. *Comput. Struct. Biotechnol. J.* 21, 3736–3745.
- Chun, Y., Kim, M., Park, J., 2002. Oxygen-dependent and-independent regulation of HIF-1 $\alpha$ . *J. Korean Med. Sci.* 17, 581.
- Chung, C., Murphy, C., Wingate, V., Pavlicek, J., Nakashima, R., Wei, W., McCarty, D., Rabinowitz, J., Barton, E., 2023. Production of rAAV by plasmid transfection induces antiviral and inflammatory responses in suspension HEK293 cells. *Mol. Ther. Methods & Clin. Dev.* 28, 272–283.
- Clausen, A., Sokol, S., 2020. Deriv: R-based symbolic differentiation. <https://CRAN.R-project.org/package=Deriv>, Deriv package version 4.1.
- Clement, N., Grieger, J., 2016. Manufacturing of recombinant adeno-associated viral vectors for clinical trials. *Mol. Ther. Methods & Clin. Dev.* 3.
- Cockcroft, S., 2021. Mammalian lipids: structure. *Synth. Funct. Essays Biochem.* 65, 813–845.
- Corcoran, S., O'Neill, L., et al., 2016. HIF1 $\alpha$  and metabolic reprogramming in inflammation. *J. Clin. Investig.* 126, 3699–3707.
- Cotner, M., Zhan, J., Zhang, Z., 2021. A computational metabolic model for engineered production of resveratrol in *Escherichia coli*. *ACS Synth. Biol.* 10, 1992–2001.
- Daskalaki, E., Pillon, N., Krook, A., Wheelock, C., Checa, A., 2018. The influence of culture media upon observed cell secretome metabolite profiles: The balance between cell viability and data interpretability. *Anal. Chim. Acta* 1037, 338–350.
- Desouki, A., Jarre, F., Gelius-Dietrich, G., Lercher, M., 2015. CycleFreeFlux: efficient removal of thermodynamically infeasible loops from flux distributions. *Bioinform.* 31, 2159–2165.
- Dietmair, S., Hodson, M., Quek, L., Timmins, N., Gray, P., Nielsen, L., 2012. A multi-omics analysis of recombinant protein production in Hek293 cells. *PLoS One.*
- Edwards, J., Palsson, B., 1999. Systems properties of the *Haemophilus influenzae* Rd metabolic genotype. *J. Biol. Chem.* 274, 17410–17416.
- Ezeonwumelu, I., Garcia-Vidal, E., Ballana, E., 2021. JAK-STAT pathway: A novel target to tackle viral infections. *Viruses* 13, 2379.
- Ezzeddini, R., Taghikhani, M., Somi, M., Samadi, N., Rasaee, M., 2019. Clinical importance of FASN in relation to HIF-1 $\alpha$  and SREBP-1c in gastric adenocarcinoma. *Life Sci.* 224, 169–176.
- Feudner, E., Alwis, M.De., Thrasher, A., Ali, R., Fauser, S., 2001. Optimization of recombinant Adeno-Associated Virus production using an herpes simplex virus amplicon system. *J. Virol. Methods* 96, 97–105.
- Frezza, C., Zheng, L., Folger, O., Rajagopalan, K., MacKenzie, E., Jerby, L., Micaroni, M., Chaneton, B., Adam, J., Hedley, A., et al., 2011. Haem oxygenase is synthetically lethal with the tumour suppressor fumarate hydratase. *Nat.* 477, 225–228.
- Garcia-Bermudez, J., Baudrier, L., La, K., Zhu, X., Fidelin, J., Sviderskiy, V., Papanikolaou, T., Molina, H., Snuderl, M., Lewis, C., et al., 2018. Aspartate is a limiting metabolite for cancer cell proliferation under hypoxia and in tumours. *Nat. Cell Biol.* 20, 775–781.
- Giallongo, S., Costa, F., Longhitano, L., Giallongo, C., Ferrigno, J., Tropea, E., Vicario, N., Li Volti, G., Parenti, R., Barbagallo, I., et al., 2023. The pleiotropic effects of fumarate: From mitochondrial respiration to epigenetic rewiring and DNA repair mechanisms. *Metab.* 13, 880.
- Gotsmy, M., Erian, A., Marx, H., Pflügl, S., Zanghellini, J., 2024. Predictive dynamic control accurately maps the design space for 2, 3-butanediol production. *Comput. Struct. Biotechnol. J.* 23, 3850–3858.
- Gotsmy, M., Strobl, F., Weiß, F., Gruber, P., Kraus, B., Mairhofer, J., Zanghellini, J., 2023. Sulfate limitation increases specific plasmid DNA yield and productivity in *E. coli* fed-batch processes. *Microb. Cell Factories* 22, 242.
- Graham, F., Smiley, J., Russell, W., Nairn, R., 1977. Characteristics of a human cell line transformed by DNA from human adenovirus type 5. *J. Gen. Virol.* 36, 59–72.
- Gu, C., Kim, G., Kim, W., Kim, H., Lee, S., 2019. Current status and applications of genome-scale metabolic models. *Genome Biol.* 20, 1–18.
- Gurazada, S., Kennedy, H., Braatz, R., Mehrman, S., Polson, S., Rombel, I., 2024. HEK-omics: The promise of omics to optimize HEK293 for recombinant Adeno-Associated Virus (rAAV) gene therapy manufacturing. *Biotechnol. Adv.* 108506.
- Hayashi, Y., Yokota, A., Harada, H., Huang, G., 2019. Hypoxia/pseudohypoxia-mediated activation of hypoxia-inducible factor-1 $\alpha$  in cancer. *Cancer Sci.* 110, 1510–1517.
- Hiroi, M., Mori, K., Sakaeda, Y., Shimada, J., Ohmori, Y., 2009. STAT1 represses hypoxia-inducible factor-1-mediated transcription. *Biochem. Biophys. Res. Commun.* 387, 806–810.
- Hooftman, A., Peace, C., Ryan, D., Day, E., Yang, M., McGettrick, A., Yin, M., Montano, E., Huo, L., Toller-Kawahisa, J., et al., 2023. Macrophage fumarate hydratase restrains mRNA-mediated interferon production. *Nat.* 615, 490–498.
- Hu, X., Li, J., Fu, M., Zhao, X., Wang, W., 2021. The JAK/STAT signaling pathway: from bench to clinic. *Signal Transduct. Target. Ther.* 6, 402.
- Huang, Z., Xu, J., Yongky, A., Morris, C., Polanco, A., Reily, M., Borys, M., Li, Z., Yoon, S., 2020. CHO cell productivity improvement by genome-scale modeling and pathway analysis: Application to feed supplements. *Biochem. Eng. J.* 160, 107638.
- Im, D., Muzyczka, N., 1990. The AAV origin binding protein Rep68 is an ATP-dependent site-specific endonuclease with DNA helicase activity. *Cell.* 61, 447–457.
- Jang, M., Pete, E., Bruheim, P., 2022. The impact of serum-free culture on HEK293 cells: From the establishment of suspension and adherent serum-free adaptation cultures to the investigation of growth and metabolic profiles. *Front. Bioeng. Biotechnol.* 10, 964397.
- Jerby, L., Shlomi, T., Ruppin, E., 2010. Computational reconstruction of tissue-specific metabolic models: application to human liver metabolism. *Mol. Syst. Biol.* 6, 401.
- Jeridi, A., Kapellos, T., Yildirim, A., 2023. Fumarate hydratase: a new checkpoint of metabolic regulation in inflammatory macrophages. *Signal Transduct. Target. Ther.* 8, 332.
- Jiang, P., Du, W., Wu, M., 2014. Regulation of the pentose phosphate pathway in cancer. *Protein & Cell.* 5, 592–602.
- Jin, L., Zhou, Y., 2019. Crucial role of the pentose phosphate pathway in malignant tumors. *Oncol. Lett.* 17, 4213–4221.
- Joe, C., Jiang, J., Linke, T., Li, Y., Fedosyuk, S., Gupta, G., Berg, A., Segireddy, R., Mainwaring, D., Joshi, A., et al., 2022. Manufacturing a chimpanzee adenovirus-vectored SARS-CoV-2 vaccine to meet global needs. *Biotechnol. Bioeng.* 119, 48.
- Kahlig, C., Moser, S., Micutkova, L., Grillari, J., Kraus, B., Hernandez Bort, J., 2024. Enhancement of rAAV titers via inhibition of the interferon signaling cascade in transfected HEK293 suspension cultures. *Biotechnol. J.* 19, 2300672.
- Kappler, M., Pabst, U., Weinholdt, C., Taubert, H., Rot, S., Kaune, T., Kotrba, J., Porsch, M., Güttler, A., Bache, M., et al., 2019. Causes and consequences of a glutamine induced normoxic HIF1 activity for the tumor metabolism. *Int. J. Mol. Sci.* 20, 4742.
- Kim, J., Tchernyshyov, I., Semenza, G., Dang, C., 2006. HIF-1-mediated expression of pyruvate dehydrogenase kinase: a metabolic switch required for cellular adaptation to hypoxia. *Cell Metab.* 3, 177–185.
- Koh, M., Spivak-Kroizman, T., Venturini, S., Welsh, S., Williams, R., Kirkpatrick, D., Powis, G., 2008. Molecular mechanisms for the activity of PX-478, an antitumor inhibitor of the hypoxia-inducible factor-1 $\alpha$ . *Mol. Cancer Ther.* 7, 90–100.
- Landgraf, A., Lee, Y., 2020. Dimensionality reduction for binary data through the projection of natural parameters. *J. Multivar. Anal.* 180, 104668.
- Leone, A., Roca, M., Ciardiello, C., Costantini, S., Budillon, A., 2017. Oxidative stress gene expression profile correlates with cancer patient poor prognosis: identification of crucial pathways might select novel therapeutic approaches. *Oxidative Med. Cell. Longev.* 2017, 2597581.
- Liang, S., Dong, S., Liu, W., Wang, M., Tian, S., Ai, Y., Wang, H., 2022. Accumulated ROS activates HIF-1 $\alpha$ -induced glycolysis and exerts a protective effect on sensory hair cells against noise-induced damage. *Front. Mol. Biosci.* 8, 806650.
- Lin, Y., Boone, M., Meuris, L., Lemmens, I., Roy, N.Van., Soete, A., Reumers, J., Moisse, M., Plaisance, S., Drmanac, R., et al., 2014. Genome dynamics of the human embryonic kidney 293 lineage in response to cell biology manipulations. *Nat. Commun.* 5, 4767.
- Lu, M., Lee, Z., Hu, W., 2024. Multi-omics kinetic analysis of recombinant Adeno-Associated Virus production by plasmid transfection of HEK293 cells. *Biotechnol. Prog.* e3428.
- Lundberg, S., 2017. A unified approach to interpreting model predictions. *arXiv Preprint arXiv:1705.07874*.
- Ma, X., Dong, Z., Liu, J., Ma, L., Sun, X., Gao, R., Pan, L., Zhang, J., An, J., Hu, K., et al., 2022. beta-Hydroxybutyrate exacerbates hypoxic injury by inhibiting HIF-1 $\alpha$ -dependent glycolysis in cardiomyocytes—adding fuel to the fire? *Cardiovasc. Drugs Ther.* 1–15.
- Madden, E., Logue, S., Healy, S., Manie, S., Samali, A., 2019. The role of the unfolded protein response in cancer progression: From oncogenesis to chemoresistance. *Biol. Cell* 111, 1–17.
- Malm, M., Kuo, C., Barzadd, M., Mebrahtu, A., Wistbacka, N., Razavi, R., Volk, A., Lundqvist, M., Kotol, D., Tegel, H., et al., 2022. Harnessing secretory pathway differences between HEK293 and CHO to rescue production of difficult to express proteins. *Metab. Eng.* 72, 171–187.
- Malm, M., Saghaleyni, R., Lundqvist, M., Giudici, M., Chotteau, V., Field, R., Varley, P., Hatton, D., Grassi, L., Svensson, T., et al., 2020. Evolution from adherent to suspension: systems biology of HEK293 cell line development. *Sci. Rep.* 10, 18996.
- Manuel, A., Walla, M., Dorn, M., Tanis, R., Piroli, G., Frizzell, N., 2020. Fumarate and oxidative stress synergize to promote stability of C/EBP homologous protein in the adipocyte. *Free. Radic. Biol. Med.* 148, 70–82.
- Martinez-Monge, I., Albiol, J., Lecina, M., Liste-Calleja, L., Miret, J., Sola, C., Cairo, J., 2019. Metabolic flux balance analysis during lactate and glucose concomitant consumption in HEK293 cell cultures. *Biotechnol. Bioeng.* 116, 388–404.
- Mary, B., Maurya, S., Arumugam, S., Kumar, V., Jayandharan, G., 2019. Post-translational modifications in capsid proteins of recombinant Adeno-Associated Virus (AAV) 1-rh10 serotypes. *FEBS J.* 286, 4964–4981.
- Meer, G., Kroon, A., 2011. Lipid map of the mammalian cell. *J. Cell Sci.* 124, 5–8.
- Megchelenbrink, W., Huynen, M., Marchiori, E., 2014. optGpSampler: an improved tool for uniformly sampling the solution-space of genome-scale metabolic networks. *PLoS One* 9, e86587.
- Meier, A., Fraefel, C., Seyffert, M., 2020. The interplay between Adeno-Associated Virus and its helper viruses. *Viruses* 12, 662.
- Mendes, J., Fernandes, B., Pineda, E., Kudugunti, S., Bransby, M., Gantier, R., Peixoto, C., Alves, P., Roldão, A., Silva, R., 2022. AAV process intensification by perfusion bioreaction and integrated clarification. *Front. Bioeng. Biotechnol.* 10, 1020174.

- Mills, E., Kelly, B., Logan, A., Costa, A., Varma, M., Bryant, C., Tourlomousis, P., Däbritz, J., Gottlieb, E., Latorre, I., et al., 2016. Succinate dehydrogenase supports metabolic repurposing of mitochondria to drive inflammatory macrophages. *Cell* 167, 457–470.
- Moço, P., Xu, X., Silva, C., Kamen, A., 2023. Production of adeno-associated viral vector serotype 6 by triple transfection of suspension HEK293 cells at higher cell densities. *Biotechnol. J.* 18, 2300051.
- Mulcrone, P., Lam, A., Frabutt, D., Zhang, J., Chrzanowski, M., Herzog, R., Xiao, W., 2023. Chemical modification of AAV9 capsid with N-ethyl maleimide alters vector tissue tropism. *Sci. Rep.* 13, 8436.
- Nagao, A., Kobayashi, M., Koyasu, S., Chow, C., Harada, H., 2019. HIF-1-dependent reprogramming of glucose metabolic pathway of cancer cells and its therapeutic significance. *Int. J. Mol. Sci.* 20, 238.
- Nash, K., Chen, W., Muzyczka, N., 2008. Complete in vitro reconstitution of Adeno-Associated Virus DNA replication requires the minichromosome maintenance complex proteins. *J. Virol.* 82, 1458–1464.
- Newman, J., Verdin, E., 2014. Beta-hydroxybutyrate: much more than a metabolite. *Diabetes Res. Clin. Pr.* 106, 173–181.
- Nguyen, T., Sha, S., Hong, M., Maloney, A., Barone, P., Neufeld, C., Wolfrum, J., Springs, S., Sinskey, A., Braatz, R., 2021. Mechanistic model for production of recombinant Adeno-Associated Virus via triple transfection of HEK293 cells. *Mol. Ther. Methods & Clin. Dev.* 21, 642–655.
- Nie, Y., Pan, H., Li, Q., Na, H., Figueroa, B., Vincent, K., 2024. Characterization of the function of Adenovirus L4 gene products and their impact on AAV vector production. *Mol. Ther. Methods Clin. Dev.* 32.
- Ooi, A., Furge, K., 2012. Fumarate hydratase inactivation in renal tumors: HIF1alpha, NRE2, and cryptic targets of transcription factors. *Chin. J. Cancer* 31, 413.
- O'Shea, J., Schwartz, D., Villarino, A., Gadina, M., McClnnes, I., Laurence, A., 2015. The JAK-STAT pathway: impact on human disease and therapeutic intervention. *Annu. Rev. Med.* 66, 311–328.
- Pan, X., Dalm, C., Wijffels, R., Martens, D., 2017. Metabolic characterization of a CHO cell size increase phase in fed-batch cultures. *Appl. Microbiol. Biotechnol.* 101, 8101–8113.
- Pedregosa, F., Varoquaux, G., Gramfort, A., Michel, V., Thirion, B., Grisel, O., Blondel, M., Prettenhofer, P., Weiss, R., Dubourg, V., Vanderplas, J., Passos, A., Cournapeau, D., Brucher, M., Perrot, M., Duchesnay, E., 2011. Scikit-learn: Machine learning in Python. *J. Mach. Learn. Res.* 12, 2825–2830.
- Pérez-Fernández, B., Cossio-Díaz, J., Boggiano, T., León, K., Mulet, R., 2021. In-silico media optimization for continuous cultures using genome scale metabolic networks: The case of CHO-K1. *Biotechnol. Bioeng.* 118, 1884–1897.
- Pistek, M., Kahlig, C., Hackl, M., Unterthurner, S., Kraus, B., Grabherr, R., Grillari, J., Hernandez Bort, J., 2023. Comprehensive mRNA-sequencing-based characterization of three HEK-293 cell lines during an rAAV production process for gene therapy applications. *Biotechnol. J.* 18, 2200513.
- Prashad, K., Mehra, S., 2015. Dynamics of unfolded protein response in recombinant CHO cells. *Cytotechnology* 67, 237–254.
- Qi, J., Gan, L., Fang, J., Zhang, J., Yu, X., Guo, H., Cai, D., Cui, H., Gou, L., Deng, J., et al., 2022. Beta-hydroxybutyrate: a dual function molecular and immunological barrier function regulator. *Front. Immunol.* 13, 805881.
- Quek, L., Dietmair, S., Hanscho, M., Martínez, V., Borth, N., Nielsen, L., 2014. Reducing recon 2 for steady-state flux analysis of HEK cell culture. *J. Biotechnol.* 184, 172–178.
- Robinson, J., Kocabaş, P., Wang, H., Cholley, P., Cook, D., Nilsson, A., Anton, M., Ferreira, R., Domenzain, I., Billa, V. and others, 2020. An Atlas of human metabolism. *Sci. Signal.* 13, eaaz1482.
- Rocklin, M., 2015. Dask: Parallel computation with blocked algorithms and task scheduling. In: *Proceedings of the 14th Python in Science Conference*.
- Rustin, P., Munnich, A., Rötig, A., 2002. Succinate dehydrogenase and human diseases: new insights into a well-known enzyme. *Eur. J. Hum. Genet.* 10, 289–291.
- Salmikangas, P., Carlsson, B., Klumb, C., Reimer, T., Thirstrup, S., 2023. Potency testing of cell and gene therapy products. *Front. Med.* 10, 1190016.
- Salvy, P., Fengos, G., Ataman, M., Pathier, T., Soh, K., Hatzimanikatis, V., 2019. pyTFA and matTFA: a Python package and a Matlab toolbox for thermodynamics-based flux analysis. *Bioinform.* 35, 167–169.
- Samulski, R., Muzyczka, N., 2014. AAV-mediated gene therapy for research and therapeutic purposes. *Annu. Rev. Virol.* 1, 427–451.
- Schlögel, G., Lück, R., Kittler, S., Spadiut, O., Kopp, J., Zanghellini, J., Gotsmy, M., 2024. Optimizing bioprocessing efficiency with OptFed: Dynamic nonlinear modeling improves product-to-biomass yield. *Comput. Struct. Biotechnol. J.* 23, 3651–3661.
- Schoeny, H., Rampler, E., Hermann, G., Grienke, U., Rollinger, J., Koellensperger, G., 2020. Preparative supercritical fluid chromatography for lipid class fractionation—a novel strategy in high-resolution mass spectrometry based lipidomics. *Anal. Bioanal. Chem.* 412, 2365–2374.
- Schultz, A., Qutub, A., 2016. Reconstruction of tissue-specific metabolic networks using CORDA. *PLoS Comput. Biol.* 12, e1004808.
- Schwartz, D., Powis, G., Thitai-Kumar, A., He, Y., Bankson, J., Williams, R., Lemos, R., Oh, J., Volgin, A., Soghomonyan, S., et al., 2009. The selective hypoxia inducible factor-1 inhibitor PX-478 provides in vivo radiosensitization through tumor stromal effects. *Mol. Cancer Ther.* 8, 947–958.
- Seabold, S., Perktold, J., 2010. statsmodels: Econometric and statistical modeling with Python. In: *9th Python In Science Conference*.
- Semenza, G., 2003. Targeting HIF-1 for cancer therapy. *Nat. Rev. Cancer* 3, 721–732.
- Shanmugasundaram, K., Nayak, B., Shim, E., Livi, C., Block, K., Sudarshan, S., 2014. The oncometabolite fumarate promotes pseudohypoxia through noncanonical activation of NF-KB signaling. *J. Biol. Chem.* 289, 24691–24699.
- Shina, S., Nagao, N., Hasegawa, J., Sato, T., Mori, C., Ohtaki, K., Kubodera, K., Yamashita, Y., Tanabe, K., Kawano, Y., et al., 2022. Effect of alcohol on productivity and quality of Adeno-Associated Virus 2 in HEK293 cells. *J. Biosci. Bioeng.* 134, 338–347.
- Strasser, L., Boi, S., Guapo, F., Donohue, N., Barron, N., Rainbow-Fletcher, A., Bones, J., 2021. Proteomic landscape of Adeno-Associated Virus (AAV)-producing HEK293 cells. *Int. J. Mol. Sci.* 22, 11499.
- Swainston, N., Smallbone, K., Hefzi, H., Dobson, P., Brewer, J., Hanscho, M., Zielinski, D., Ang, K., Gardiner, N., Gutierrez, J., et al., 2016. Recon 2.2: from reconstruction to model of human metabolism. *Metabolomics* 12, 1–7.
- Szélliová, D., Iurashev, D., Ruckerbauer, D., Koellensperger, G., Borth, N., Melcher, M., Zanghellini, J., 2021. Error propagation in constraint-based modeling of Chinese hamster ovary cells. *Biotechnol. J.* 16, 2000320.
- Szélliová, D., Ruckerbauer, D., Galleguillos, S., Petersen, L., Natter, K., Hanscho, M., Troyer, C., Causon, T., Schoeny, H., Christensen, H., et al., 2020. What CHO is made of: Variations in the biomass composition of Chinese hamster ovary cell lines. *Metab. Eng.* 61, 288–300.
- Thai, M., Graham, N., Braas, D., Nehil, M., Komisopoulou, E., Kurdistani, S., McCormick, F., Graeber, T., Christofk, H., 2014. Adenovirus E4ORF1-induced MYC activation promotes host cell anabolic glucose metabolism and virus replication. *Cell Metab.* 19, 694–701.
- Thaker, S., Ch'ng, J., Christofk, H., 2019. Viral hijacking of cellular metabolism. *BMC Biol.* 17, 1–15.
- Thiele, I., Swainston, N., Fleming, R., Hoppe, A., Sahoo, S., Aurich, M., Haraldsdottir, H., Mo, M., Rolfsson, O., Stobbe, M., et al., 2013. A community-driven global reconstruction of human metabolism. *Nat. Biotechnol.* 31, 419–425.
- Thomas, P., Smart, T., 2005. HEK293 cell line: a vehicle for the expression of recombinant proteins. *J. Pharmacol. Toxicol. Methods* 51, 187–200.
- Tokuda, K., Baron, B., Yamashiro, C., Kuramitsu, Y., Kitagawa, T., Kobayashi, M., Sonoda, K., Kimura, K., 2020. Up-regulation of the pentose phosphate pathway and HIF-1alpha expression during neural progenitor cell induction following glutamate treatment in rat ex vivo retina. *Cell Biol. Int.* 44, 137–144.
- Trejo-Solis, C., Castillo-Rodriguez, R., Serrano-Garcia, N., Silva-Adaya, D., Vargas-Cruz, S., Chavez-Cortez, E., Gallardo-Perez, J., Zavala-Vega, S., Cruz-Salgado, A., Magana-Maldonado, R., 2024. Metabolic Roles of HIF1, c-Myc, and p53 in Glioma Cells. *Metab.* 14, 249.
- Tsuji, T., Morita, S., Nakamura, Y., Ikeda, Y., Kambe, T., Terada, T., 2021. Alterations in cellular and organellar phospholipid compositions of HepG2 cells during cell growth. *Sci. Rep.* 11, 2731.
- Tyrakis, P., Yurkovich, M., Sciacovelli, M., Papachristou, E., Bridges, H., Gaude, E., Schreiner, A., D'Santos, C., Hirst, J., Hernandez-Fernaund, J., et al., 2017. Fumarate hydratase loss causes combined respiratory chain defects. *Cell Rep.* 21, 1036–1047.
- Vailionis, J., Zhao, W., Zhang, K., Rodionov, D., Lipscomb, G., Tanwee, T., O'Quinn, H., Bing, R., Kelly, R., Adams, M., et al., 2023. Optimizing strategies for bio-based ethanol production using genome-scale metabolic modeling of the hyperthermophilic archaeon, *pyrococcus furiosus*. *Appl. Environ. Microbiol.* 89, e00563-23.
- Van Meer, G., Voelker, D., Feigenson, G., 2008. Membrane lipids: where they are and how they behave. *Nat. Rev. Mol. Cell Biol.* 9, 112–124.
- Vance, J., 2008. Phosphatidylserine and phosphatidylethanolamine in mammalian cells: two metabolically related aminophospholipids. *J. Lipid Res.* 49, 1377–1387.
- Vance, J., 2015. Phospholipid synthesis and transport in mammalian cells. *Traffic* 16, 1–18.
- Virtanen, P., Gommers, R., Oliphant, T., Haberland, M., Reddy, T., Cournapeau, D., Burovski, E., Peterson, P., Weckesser, W., Bright, J., Van der Walt, S., Brett, M., Wilson, J., Millman, K., Mayorov, N., Nelson, A., Jones, E., Kern, R., Larson, E., Carey, C., Polat, I., Feng, Y., Moore, E., VanderPlas, J., Laxalde, D., Perktold, J., Cimrman, R., Henriksen, I., Quintero, E., Harris, C., Archibald, A., Ribeiro, A., Pedregosa, F., Van Mulbregt, P., SciPy 1.0 Contributors, 2020. SciPy 1.0: Fundamental algorithms for scientific computing in Python. *Nat. Methods* 17, 261–272.
- Vlassis, N., Pacheco, M., Sauter, T., 2014. Fast reconstruction of compact context-specific metabolic network models. *PLoS Comput. Biol.* 10, e1003424.
- Wang, Y., Fu, Q., Lee, Y., Sha, S., Yoon, S., 2023. Transcriptomic features reveal molecular signatures associated with recombinant Adeno-Associated Virus production in HEK293 cells. *Biotechnol. Prog.* 39, e3346.
- Wang, J., Gessler, D., Zhan, W., Gallagher, T., Gao, G., 2024. Adeno-Associated Virus as a delivery vector for gene therapy of human diseases. *Signal Transduct. Target. Ther.* 9, 78.
- Wang, T., Liu, H., Lian, G., Zhang, S., Wang, X., Jiang, C., 2017. HIF1alpha-induced glycolysis metabolism is essential to the activation of inflammatory macrophages. *Mediat. Inflamm.* 2017, 9029327.
- Welsh, S., Williams, R., Kirkpatrick, L., Paine-Murrieta, G., Powis, G., 2004. Antitumor activity and pharmacodynamic properties of PX-478, an inhibitor of hypoxia-inducible factor-1alpha. *Mol. Cancer Ther.* 3, 233–244.

- Xu, L., Ishikawa, H., Zhou, Y., Kobayashi, T., Shozu, M., 2022. Antitumor effect of the selective hypoxia-inducible factor-1 inhibitors echinomycin and PX-478 on uterine fibroids. *F & S Sci.* 3, 187–196.
- Xu, X., Zur Hausen, A., Coy, J., Löchelt, M., 2009. Transketolase-like protein 1 (TKTL1) is required for rapid cell growth and full viability of human tumor cells. *Int. J. Cancer* 124, 1330–1337.
- Yang, Y., Lane, A., Ricketts, C., Sourbier, C., Wei, M., Shuch, B., Pike, L., Wu, M., Rouault, T., Boros, L., et al., 2013. Metabolic reprogramming for producing energy and reducing power in fumarate hydratase null cells from hereditary leiomyomatosis renal cell carcinoma. *PLoS One* 8, e72179.
- Yang, M., Soga, T., Pollard, P., Adam, J., 2012. The emerging role of fumarate as an oncometabolite. *Front. Oncol.* 2, 85.
- Zecchini, V., Paupe, V., Herranz-Montoya, I., Janssen, J., Wortel, I., Morris, J., Ferguson, A., Chowdury, S., Segarra-Mondejar, M., Costa, A., et al., 2023. Fumarate induces vesicular release of mtDNA to drive innate immunity. *Nat.* 615, 499–506.
- Zeh, N., Schlossbauer, P., Raab, N., Klingler, F., Handrick, R., Otte, K., 2021. Cell line development for continuous high cell density biomanufacturing: Exploiting hypoxia for improved productivity. *Metab. Eng. Commun.* 13, e00181.
- Zehetner, L., Széliyová, D., Kraus, B., Bort, J., Hernandez, J., Zanghellini, J., 2024. Logistic PCA explains differences between genome-scale metabolic models in terms of metabolic pathways. *PLoS Comput. Biol.* 20, e1012236.
- Zehetner, L., Széliyová, D., Kraus, B., Graninger, M., Zanghellini, J., Hernandez Bort, J., 2023. Optimizing VLP production in gene therapy: Opportunities and challenges for in silico modeling. *Biotechnol. J.* 18, 2200636.
- Zeidan, E., Hossain, M., El-Daly, M., Abourehab, M., Khalifa, M., Taye, A., 2022. Mitochondrial regulation of the hypoxia-inducible factor in the development of pulmonary hypertension. *J. Clin. Med.* 11, 5219.
- Zhang, Y., Baycin-Hizal, D., Kumar, A., Priola, J., Bahri, M., Heffner, K., Wang, M., Han, X., Bowen, M., Betenbaugh, M., 2017. High-throughput lipidomic and transcriptomic analysis to compare SP2/0, CHO, and HEK-293 mammalian cell lines. *Anal. Chem.* 89, 1477–1485.
- Zhang, Y., Wang, S., Hu, H., Li, X., 2022c. A systematic study of HIF1A cofactors in hypoxic cancer cells. *Sci. Rep.* 12, 18962.
- Zheng, L., Cardaci, S., Jerby, L., MacKenzie, E., Sciacovelli, M., Johnson, T., Gaude, E., King, A., Leach, J., Edrada-Ebel, R., et al., 2015. Fumarate induces redox-dependent senescence by modifying glutathione metabolism. *Nat. Commun.* 6, 6001.
- Zhu, Y., Zang, Y., Zhao, F., Li, Z., Zhang, J., Fang, L., Li, M., Xing, L., Xu, Z., Yu, J., 2017. Inhibition of HIF-1 $\alpha$  by PX-478 suppresses tumor growth of esophageal squamous cell cancer in vitro and in vivo. *Am. J. Cancer Res.* 7, 1198.